Cell Insight 3 (2024) 100183

Contents lists available at ScienceDirect

Cell Insight

journal homepage: www.journals.elsevier.com/cell-insight

Research Article

ATR/Chk1 interacting lncRNA modulates DNA damage response to induce breast cancer chemoresistance

Rong Luo [a,b,c,1], Jiannan Wu [a,b,1], Xueman Chen [a,b,1], Yulan Liu [a,b], Dequan Liu [c], Erwei Song [a,b,*], Man-Li Luo [a,d,**]

[a] Guangdong Provincial Key Laboratory of Malignant Tumor Epigenetics and Gene Regulation, Guangdong-Hong Kong Joint Laboratory for RNA Medicine, Sun Yat-Sen Memorial Hospital, Sun Yat-Sen University, Guangzhou, China
[b] Breast Tumor Center, Sun Yat-Sen Memorial Hospital, Sun Yat-Sen University, Guangzhou, China
[c] The First Department of Breast Cancer, The Third Affiliated Hospital, Kunming Medical University, Kunming, China
[d] Medical Research Center, Sun Yat-Sen Memorial Hospital, Sun Yat-Sen University, Guangzhou, China

HIGHLIGHTS

- LncRNA ACIL promotes ATR-Chk1 activation in the response to DNA damage.
- ACIL interacts with both ATR and Chk1 to enhance Chk1 phosphorylation.
- ACIL induces chemoresistance and correlates with poor outcome of breast cancer patients.

GRAPHICAL ABSTRACT

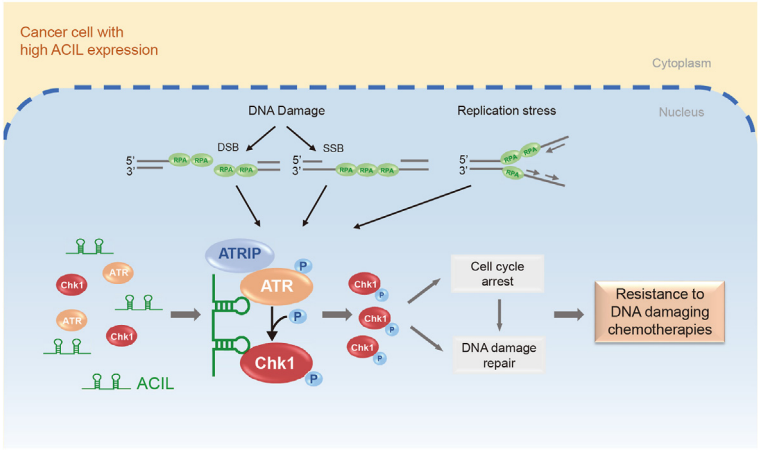

ARTICLE INFO

Keywords:
Long noncoding RNA
Chemotherapy resistance
DNA damage response
ATR
Chk1

ABSTRACT

The ATR-Chk1 pathway is essential in cellular responses to DNA damage and replication stress, whereas the role of long noncoding RNAs (lncRNAs) in regulating this pathway remains largely unknown. In this study, we identify an ATR and Chk1 interacting lncRNA (ACIL, also known as LRRC75A-AS1 or SNHG29), which promotes the phosphorylation of Chk1 by ATR upon DNA damages. High ACIL levels are associated with chemoresistance to DNA damaging agents and poor outcome of breast cancer patients. ACIL knockdown sensitizes breast cancer cells to DNA damaging drugs *in vitro* and *in vivo*. ACIL protects cancer cells against DNA damages by inducing cell cycle arrest, stabilizing replication forks and inhibiting unscheduled origin firing, thereby guarding against replication catastrophe and contributing to DNA damage repair. These findings demonstrate a lncRNA-dependent mechanism

* Corresponding author. Sun Yat-Sen Memorial Hospital, Sun Yat-Sen University, Guangzhou, 510120, China.
** Corresponding author. Sun Yat-Sen Memorial Hospital, Sun Yat-Sen University, Guangzhou, 510120, China.
E-mail addresses: songew@mail.sysu.edu.cn (E. Song), luomli@mail.sysu.edu.cn (M.-L. Luo).
[1] These authors contributed equally to this work.

https://doi.org/10.1016/j.cellin.2024.100183
Received 27 June 2024; Received in revised form 10 July 2024; Accepted 10 July 2024
Available online 14 July 2024

of activating the ATR-Chk1 pathway and highlight the potential of utilizing ACIL as a predictive biomarker for chemotherapy sensitivity, as well as targeting ACIL to reverse chemoresistance in breast cancer.

1. Introduction

Genomic instability is an enabling characteristic and evolving hallmark of cancer (Hanahan, 2022). Although resultant genetic alterations accompanying with dysfunction of the DNA damage response (DDR) pathways drive malignant progression, they also renders promising targets for cancer therapy (Duijf et al., 2019; Hanahan, 2022). Chemotherapeutic drugs such as anthracyclines, platinum and alkylating agents, are representative DNA damaging agents for cancer treatment (Zhou & Bartek, 2004). Anthracyclines can trap topoisomerase II (TOP2) and cause irreversible TOP2-linked DNA double-strand breaks, while platinum compounds and alkylating agents, such as cisplatin and cyclophosphamide, form bulky drug-DNA adducts, induce DNA base lesions and inter-strand or intra-strand crosslinks, all of which have been reported to activate the DDR pathway (Bruno et al., 2017; Canela et al., 2019; Crook et al., 1986). Emerging evidence has showed that the hyperactivation of DDR pathway represents one of the major mechanisms underlying chemoresistance in cancers (Mehlich et al., 2021). Tumor-targeting DNA lesions in combination with DDR inhibition has been an effective treatment and more innovative modalities to improve anti-cancer therapy (Gourley et al., 2019; Gupta et al., 2022; Pilié et al., 2019).

The ATR (ataxia-telangiectasia mutated- and Rad3-related)-Chk1 (checkpoint kinase 1) signaling pathway is critical in responding to a broad spectrum of DNA damage, especially double-strand DNA (dsDNA) end resection, single-strand DNA (ssDNA) break and replication stress (Costanzo et al., 2003; Sartori et al., 2007; Shiotani & Zou, 2009; Zou & Elledge, 2003), which result in the formation of ssDNA structures. The activation of ATR-Chk1 pathway depends on the recognition of ATRIP (ATR interacting protein) to RPA (Replication protein A) coated-ssDNA complex, which can occur in the situations of double-strand breaks (DSBs), single-strand breaks (SSBs) and DNA replication stress. During homologous recombination (HR) repair, ssDNA is generated following dsDNA end resection by the MRE11–RAD50–NBS1/NBN (MRN) complex and its interacting protein CtIP, thereby facilitating the recruitment of ATR to DSBs (Sartori et al., 2007). In unrepaired SSBs, APE2 resects SSB ends into ssDNA, allowing for the binding of RPA and activation of the ATR-Chk1 pathway (Lin et al., 2018). During replication stress, fork stalling leads to the generation of unwound ssDNA, where the binding of RPA to ssDNA contributes to fork stability and prevents fork collapse by activating ATR (Branzei & Foiani, 2010). Moreover, ATR-Chk1 pathway requires some "mediator" proteins to promote the activation, such as TopBP1, ETAA, and APE1. After being recruited by ATRIP to RPA-ssDNA complex, ATR is activated by TopBP1 that mediated by Rad9–Hus1–Rad1 (9–1–1) clamp complex, and the process required Rad17-RCF clamp loader bound DNA at early stage of DDR (Mordes et al., 2008). The RPA-binding protein ETAA1 activates ATR through a conserved ATR-activating domain to safeguard genomic stability (Lee et al., 2016). In addition, APE1 directly activates ATR to phosphorylate Chk1 by co-locating with nucleolar NPM1 and facilitating the recruitment of ATR, TopBP1 and ETAA1 in DDR (Li et al., 2022). ATR can be recruited and activated at the early stage of DDR; and Chk1, the signaling effector, is phosphorylated by ATR and then triggers cell cycle checkpoint (Bartek & Lukas, 2003). However, the regulatory mechanisms of the ATR-Chk1 signaling pathway on the chemosensitivity of breast cancer cells are not fully elucidated.

Emerging evidence has documented that long noncoding RNAs (lncRNAs) are involved in the regulation of DDR (La et al., 2023). LncRNA Discn acts as the guardian of genomic stability and fine-tunes replication protein A (RPA) availability (Wang et al., 2021). LncRNA LINP1 serves as a molecular scaffold for Ku80 and DNA-PK, which enhances the nonhomologous end joining (NHEJ) repair activity, and increases the sensitivity of cancer cells to doxorubicin and radiation (Zhang et al., 2016). Targeting the P53-dependent lncRNA NEAT1 enhances the replication stress and chemotherapy response in MCF-7 cells by weakening the ATR-Chk1 signaling (Adriaens et al., 2016). Moreover, lncRNA ANRIL promotes the radioresistance of tumor cells by binding and stabilizing ATR protein in lung cancer (Liu et al., 2021). However, in depth understanding of the mechanisms by which lncRNAs regulate the DDR signaling pathways and the role of lncRNAs in the chemoresistance of cancer cells is still lacking. In this work, through high-throughput screening of clinical tumor samples from patients receiving chemotherapy, we identified a lncRNA ACIL, whose high level was associated with the poor outcome of breast cancer patients. We demonstrated that ACIL acted as an RNA adaptor for ATR-Chk1 signaling and poses crucial impact on mediating DNA damage-induced replication stress responses in cancer cells.

2. Results

2.1. ACIL is upregulated in anthracycline-resistant breast cancer and associated with patient prognosis

To identify potential lncRNAs involved in the resistance of DNA-damaging chemotherapy, we performed two sets of lncRNA microarrays: 1) breast cancer tissues of needle biopsy before neoadjuvant chemotherapy (NAC) from three anthracycline-responding and three anthracycline-resistant patients; 2) Breast cancer tissues of needle biopsy before anthracycline-based NAC and corresponding surgical resected tumors collected from three partial response (PR) patients. By analyzing the lncRNA expression profiles, we identified 49 concordantly dysregulated lncRNAs (Fig. 1A and B) and selected the top 10 concordantly upregulated lncRNAs in anthracycline-resistant tissues for further study (Table S1). As adriamycin (ADM) was one of most important anthracyclines, we treated MDA-MB-231 cells with ADM as well as other DNA damaging agents cisplatin (CDDP) and cyclophosphamide (CPA) to verify the lncRNA microarray results. Among the top 10 lncRNAs, only ACIL (ENST00000472367, also known as LRRC75A-AS1 or SNHG29) and RP11-1379J22.5 (ENST00000503428) were significantly upregulated in response to all DNA-damaging drugs (Fig. 1C and D and Fig. S1A). As ACIL expression increased much dramatically than RP11-1379J22.5 after drug treatments, we further focused on ACIL to explore its role in breast cancer.

Next, we detected the expression of ACIL in fresh frozen human breast cancer tissues and found ACIL was significantly higher in NAC resistant breast tumors (including stable disease (SD) and progressive disease (PD)) than in the sensitive tumors (including complete response (CR) and partial response (PR)) (Fig. 1E). *In situ* hybridization (ISH) in paraffin-embedded breast cancer tissues that received NAC treatment showed that ACIL level was higher in NAC resistant tumors ($n = 108$) than that in the sensitive tumors ($n = 141$) (Fig. 1F and G). High ACIL level was associated with poor overall survival (OS) and relapse-free survival (RFS) of breast cancer patients in the Kaplan-Meier plotter database (gene chip) (https://kmplot.com) (Fig. 1H and I). When divided into the luminal, HER2+ and basal-like subtypes, ACIL expression still correlated with poor RFS in all subtypes and OS in basal-like subtype (Figs. S1B and S1C). When selecting the NAC patients only, high level of ACIL is more significantly associated with OS and RFS, with the hazard ratio up to 1.77 and 2.55, respectively (Fig. S1D). ISH analysis in breast cancer tissues from our hospital ($n = 298$) revealed that high expression of ACIL was associated with shorter overall survival in NAC patients (Fig. 1J). However, ACIL expression was not associated with tumor size, tumor stage

and tumor grade of these cancer tissues (Table S2). These data suggested that high level of ACIL was clinically relevant to poor sensitivity to NAC and worse prognosis in breast cancer patients.

In MDA-MB-231 cells, ACIL copy number upregulated by 1.5 ~ 4-fold upon exposure to various chemotherapy drugs, as determined by RT-qPCR (Fig. S1E). 5′ and 3′ rapid amplification of complementary DNA ends (RACE) followed by Sanger sequencing in MDA-MB-231 cells further confirmed that ACIL was a 1068 nt lncRNA (Fig. S1F). Comparing to the sequence in GENCODE V44, our RACE result showed that the sequence is largely the same but with some difference in the middle front segment (Table S3). There was no representative protein-coding open reading frame (ORF) longer than 300 nt in ACIL sequence, according to NCBI ORF finder (Wheeler et al., 2003). Fluorescence in situ hybridization (FISH) revealed that ACIL was localized in the nuclei of both MDA-MB-231 and MCF-7 cells (Figs. S1G and H).

2.2. *Knockdown of ACIL sensitizes breast cancer cells to DNA damaging agents*

We knocked down ACIL expression in breast cancer cell lines using locked nucleic acids (LNAs), which had a higher efficiency in silencing nuclear lncRNAs than siRNAs (Chen et al., 2022). As validated by RT-qPCR, the two LNAs targeting ACIL reduced its expression by ~70% in MDA-MB-231, Hs578T, MDA-MB-468, MDA-MB-436 and MCF-7 cells, when compared to the negative control (NC) (Fig. S2A). Silencing ACIL did not affect the growth of MDA-MB-231 and MCF-7 cells, as assessed by cell viability and Ki-67 staining (Figs. S2B–E). ACIL (LRRC75A-AS1) knockdown or overexpression also did not affect the mRNA level of LRRC75A in breast cancer cell lines (Figs. S2F and G). However, ACIL knockdown significantly reduced the half-maximal inhibitory concentration (IC50) of ADM and CDDP in MDA-MB-231, Hs578T and MDA-MB-468 cells (Fig. 2A–F). Moreover, ACIL knockdown decreased the IC50 of PARP (poly ADP-ribose polymerase) inhibitor olaparib, which could also induce DNA damages, in BRCA (breast cancer susceptibility genes)-mutant (BRCA-mut) MDA-MB-436 cells, as well as BRCA wild-type (BRCA-wt) MDA-MB-231 and MDA-MB-468 cells (Fig. 2G–I).

As assessed by Annexin V/PI staining and flow cytometry, ACIL-knockdown MDA-MB-231, Hs578T, MDA-MB-468, and MCF-7 cells exhibited a higher number of apoptotic cells than control LNA-transfected cells after exposure to CDDP (Fig. 2J-M). Olaparib-induced cell apoptosis also increased in both BRCA-mut MDA-MB-436 and BRCA-wt MDA-MB-231 cells with ACIL knockdown (Fig. 2N and O). Moreover, we utilized a CDDP-resistant (CDDP-R) subline of MDA-MB-231 to explore the impact of targeting ACIL in reducing the chemoresistance. The IC50 of CDDP-R MDA-MB-231 cells was about 8.4-folds higher than parental cells (Fig. S2H). In CDDP-R cells, a significant decrease in cell viability and a notable increase in apoptotic cells were observed upon ACIL knockdown (Fig. 2P-R). The results demonstrated

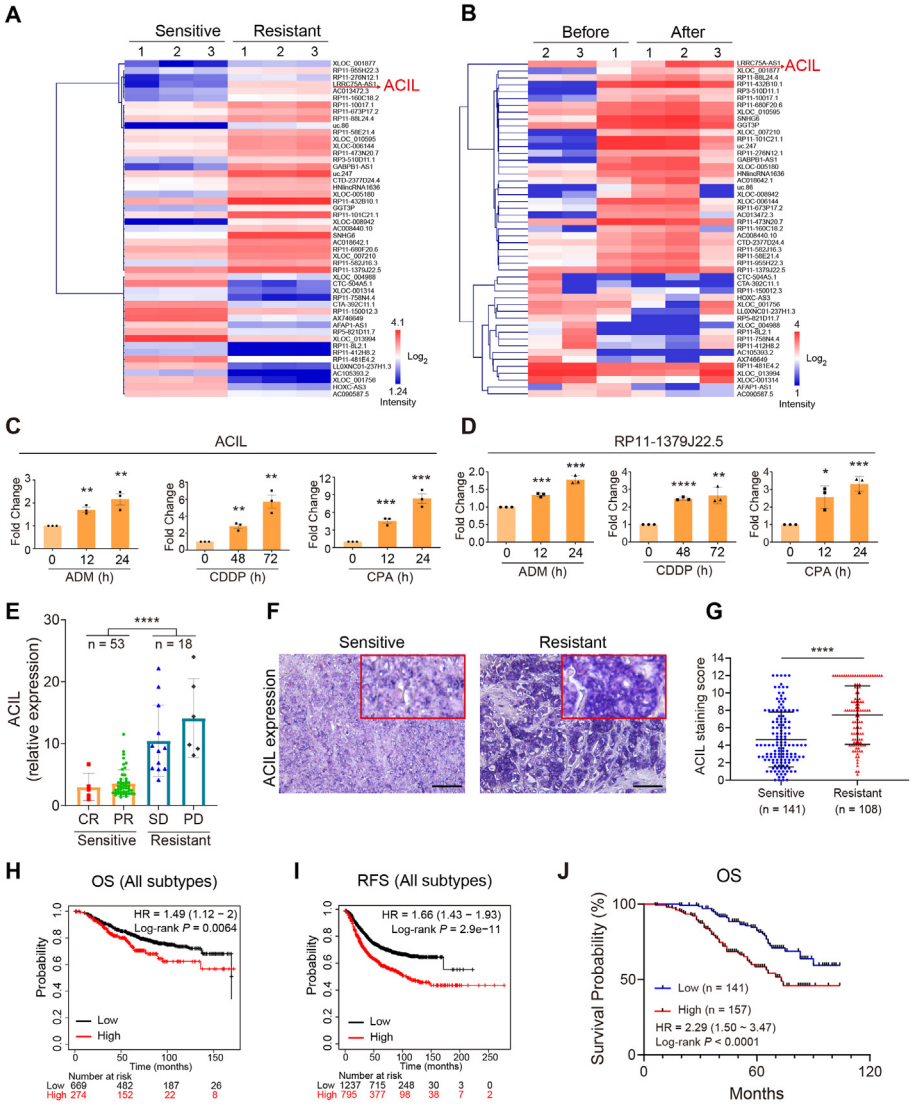

Fig. 1. ACIL is upregulated in anthracycline-resistant breast cancer tissues and associated with patient prognosis. (A) Expression profile of dysregulated lncRNAs in chemosensitive and chemoresistant breast cancer tissues. (B) Expression profile of dysregulated lncRNAs in 3 paired breast cancer tissues before and after chemotherapy. (C–D) The expression level of ACIL (C) and RP11-1379J22.5 (D) after ADM, CDDP and CPA treatment in MDA-MB-231 cells, as detected by RT-qPCR. (E) ACIL expresses higher in chemoresistant breast cancer tissues (SD, PD) than chemosensitive tissues (CR, PR), as detected by RT-qPCR. (F–G) ACIL expresses higher in chemoresistant breast cancer tissues than in chemosensitive tissues, as detected by ISH. Scale bar = 400 μm. (H–I) Kaplan–Meier survival curves for OS (H) and RFS (I) in all subtypes of breast cancer patients from the Kaplan-Meier plotter database. (J) NAC breast cancer patients with high-level ACIL expression have a shorter overall survival time. The results are presented as mean ± SEM of experimental triplicates (C, D) or mean ± SD (E, G), and *P* values were assessed by two-tailed unpaired *t*-test (C–E), two-tailed Mann-Whitney test (G), Log-rank test (H–J). *, $P < 0.05$; **, $P < 0.01$; ***, $P < 0.001$; ****, $P < 0.0001$.

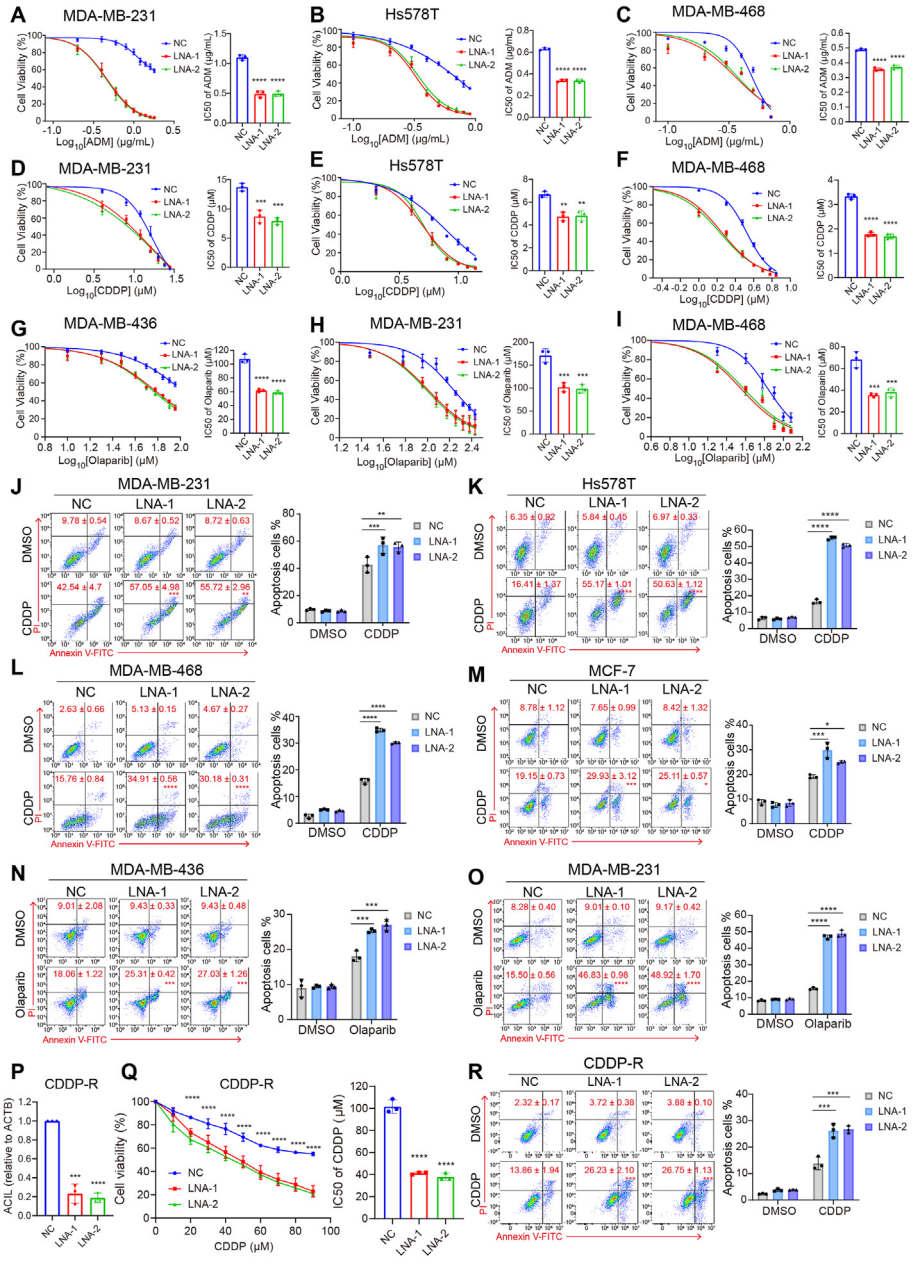

Fig. 2. Knockdown of ACIL sensitizes breast cancer cells to DNA damaging agents. (A–C) The cell viability assay shows that IC50 significantly decreases when exposed to ADM in ACIL-knockdown MDA-MB-231 (A), Hs578T (B) MDA-MB-468 (C) cells. (D–F) The cell viability assay shows that IC50 significantly decreases when exposed to CDDP in ACIL-knockdown MDA-MB-231 (D), Hs578T (E), MDA-MB-468 (F) cells. (G–I) ACIL knockdown decreases Olaparib IC50 in BRCA-mut MDA-MB-436 (G), BRCA-wt MDA-MB-231 (H) and MDA-MB-468 cells (I). (J–M) Knockdown of ACIL increases the apoptosis of MDA-MB-231 (J), Hs578T (K), MDA-MB-468 (L) and MCF-7 (M) cells when exposed to CDDP (5 μM) for 48 h. (N) Knockdown of ACIL increases the apoptosis of MDA-MB-436 when exposed to Olaparib (100 mM) for 48 h. (O) Knockdown of ACIL increases the apoptosis of MDA-MB-231 when exposed to Olaparib (150 mM) for 48 h. (P) RT-qPCR shows the ACIL knockdown efficiency in CDDP-R MDA-MB-231 cells. (Q) ACIL knockdown in CDDP-R MDA-MB-231 increases sensitivity to CDDP treatments. (R) ACIL knockdown increases the cell apoptosis of CDDP-R MDA-MB-231 cells (CDDP, 15 mM for 72 h). The results are presented as mean ± SD of experimental triplicates (A–R), and *P* values were assessed by one-way ANOVA with Dunnett's multiple comparisons test (A–R). *, $P < 0.05$; **, $P < 0.01$; ***, $P < 0.001$; ****, $P < 0.0001$.

that knockdown of ACIL enhanced the sensitivity of breast cancer cells to DNA damaging agents.

Additionally, we explored the effect of ACIL on MCF-10A cells, an immortalized mammary epithelial cell line. The growth curve indicated that ACIL knockdown did not significantly affect the proliferation of MCF-10A cells (Figs. S2I and J). The cell viability assay demonstrated that ACIL did not increase the sensitivity of MCF-10 cells to ADM and CDDP (Figs. S2K and L). These results suggest that ACIL does not exert a significant effect on the growth or chemosensitivity of MCF-10A cell line, revealing the safety of ACIL knockdown for relatively normal mammary epithelial cells.

2.3. ACIL alleviates the DNA damage accumulation in cancer cells

Next, we explored whether ACIL expression affected the extent of DNA damage. The comet assay revealed that the percentage of DNA in comet tail, the length of tail DNA, and the tail moment were consistently increased in ACIL-knockdown MDA-MB-231 cells exposed to CDDP (Fig. 3A–D). Also, the ACIL-knockdown MDA-MB-231 and Hs578T cells exhibited higher levels of γ-H2AX than the control cells when exposed to ADM (Fig. 3E and Fig. S3A). Similarly, upon exposure to olaparib, knockdown of ACIL increased the level of γ-H2AX in both BRCA-wt MDA-MB-231 and BRCA-mut MDA-MB-436 cells (Fig. 3F and Fig. S3B). When extending the treatment duration of ADM and olaparib to induce more DNA damage, ACIL-knockdown MDA-MB-231 cells also exhibited elevated levels of γ-H2AX compared to control cells (Figs. S3C and D).

The immunofluorescence staining of γ-H2AX showed that ACIL-knockdown MDA-MB-231 cells exhibited more γ-H2AX foci formation induced by Ionizing radiation (IR), as compared to NC cells, suggesting the exacerbation of DNA damage induced by ACIL knockdown (Fig. 3G and H). To expand these findings to other types of cancer cells, we silenced ACIL in HNE1 cells (a nasopharyngeal carcinoma cell line) and H1299 cells (a non-small cell lung cancer cell line). IR-induced DNA damage, as detected by the γ-H2AX level, was also higher in ACIL knockdown cells than in the NC cells (Figs. S3E–G).

In contrast, less DNA in comet tails (Fig. 3I-L) and less γ-H2AX foci

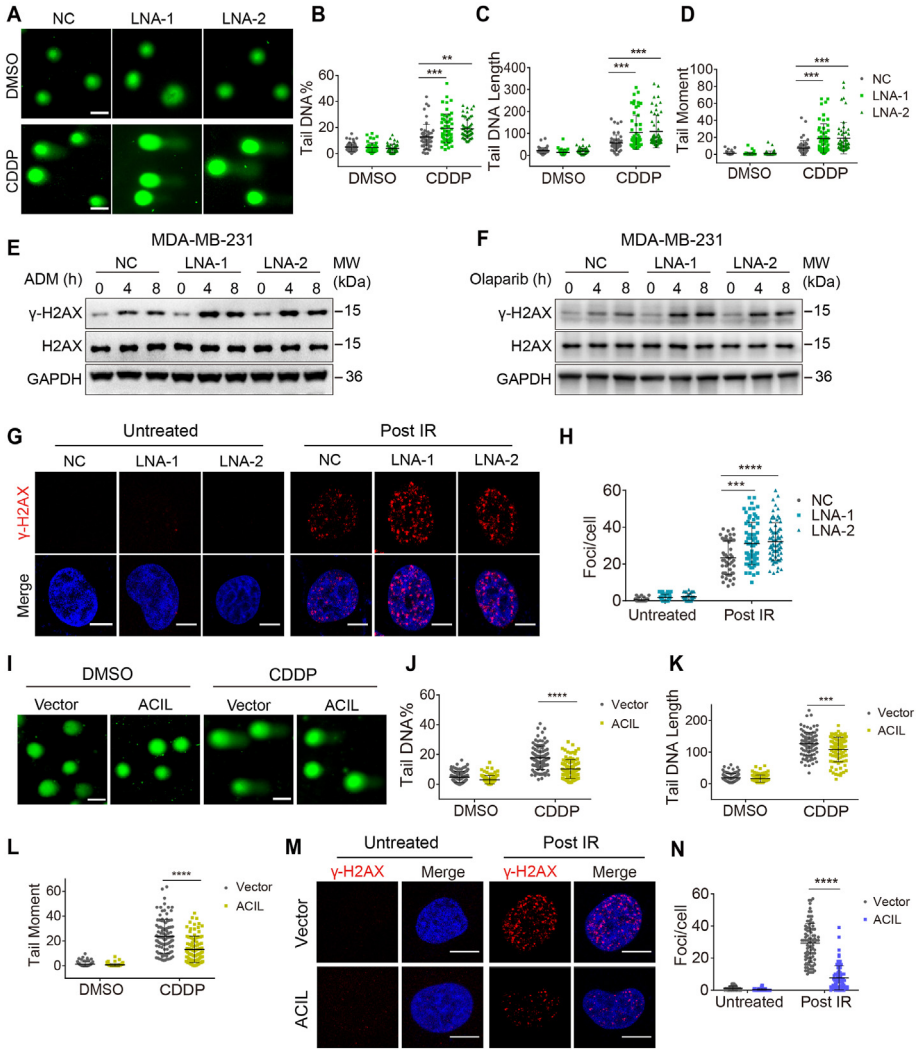

Fig. 3. ACIL alleviates the DNA damage accumulation in breast cancer cells. (A) Representative comet assay images after CDDP exposure (5 mM for 24 h) in MDA-MB-231 cells. Scale bar = 50 μm. (B–D) Statistical analysis of tail DNA (B), tail DNA length (C), and tail moment (D) in the comet assay. (E) γ-H2AX level is higher in ACIL-knockdown than NC MDA-MB-231 cells after ADM treatment (1 μg/mL). (F) γ-H2AX level is higher in ACIL-knockdown than NC MDA-MB-231 cells after Olaparib (150 mM) treatment. (G–H) Knockdown of ACIL significantly increases γ-H2AX foci formation post IR (10 Gy, repair for 2 h) in MDA-MB-231 cells. Scale bar = 10 μm. (I) Representative comet assay images of vector and ACIL overexpressed MDA-MB-231 cells after CDDP exposure (5 μM for 24 h). Scale bar = 50 μm. (J–L), Statistical analysis shows that overexpression of ACIL reduces the percentage of tail DNA (J), tail DNA length (K), and tail moment (L) in (I). (M–N) ACIL overexpressed MDA-MB-231 cells show a lower γ-H2AX foci formation post IR (10 Gy, repair for 2 h). Scale bar = 10 μm. The results are presented as mean ± SD of one representative experiment out of three (B-D, H, J-L, and N), and *P* values were assessed by one-way ANOVA with Dunnett's multiple comparisons test (B-D, H), two-tailed unpaired *t*-test (J-L, N). *, $P < 0.05$; **, $P < 0.01$; ***, $P < 0.001$; ****, $P < 0.0001$.

formation (Fig. 3M and N) were observed in ACIL-overexpressed MDA-MB-231 cells after exposure to CDDP or IR. In consistence, overexpressing ACIL in MDA-MB-231 cells decreased the level of γ-H2AX when treated with ADM (Fig. S3H). These data suggest that ACIL regulates the DNA damage response in cancer cells exposed to multiple DNA damaging agents.

2.4. *ACIL binds to Chk1 and enhances its phosphorylation*

To elucidate the mechanism by which ACIL regulated chemoresistance, we conducted RNA pulldown assay using biotinylated ACIL in MDA-MB-231 cells, followed by mass spectrometry (MS) to identify ACIL-interacting proteins. Protein bands (50–70 kDa) enriched in the ACIL pulldown complex, but not in the negative control pulldown complex were subjected to MS analysis (Fig. 4A). Among proteins identified by MS, checkpoint kinase 1 (Chk1), a conserved protein kinase central to the cell-cycle checkpoint during the DNA damage response, was identified as an ACIL-binding protein (Figs. S4A and B). Western blots following RNA pulldown further confirmed that biotinylated ACIL specifically bound to Chk1 protein (Fig. 4B). Furthermore, the binding of biotinylated ACIL and Chk1 was abolished when silencing Chk1 with siRNA (Fig. 4B). As assayed by RNA immunoprecipitation (RIP, native condition) and UV cross-linking and immunoprecipitation (CLIP, cross-linked condition) (Van Nostrand et al., 2016), ACIL was enriched with anti-Chk1 antibody by about 10-fold when compared with anti-IgG antibody (Fig. 4C and Fig. S4C), implying an interaction between ACIL and Chk1.

It has been reported that the ATM (ataxia telangiectasia-mutated)-Chk2 (checkpoint kinase 2) pathway mainly reacts with DNA double-strand breaks (DSB), while the ATR-Chk1 pathway can be activated by a wide range of DNA damages (Cimprich & Cortez, 2008). To determine which pathway ACIL was involved in, we analyzed the ATR-Chk1 and ATM-Chk2 pathways in various breast cancer cell lines treated with ADM. Immunoblotting revealed that ACIL knockdown reduced Chk1 phosphorylation in MDA-MB-231, Hs578T, and MCF-7 cells, while the phosphorylation of ATR, ATM, and Chk2 remained unaffected (Fig. 4D–I and Fig. S4D). Similar result was observed in ACIL-knockdown MDA-MB-231 cells with CDDP treatment (Fig. S4E). We found that the phosphorylation of Chk1 also decreased in olaparib-treated ACIL--knockdown BRCA-wt MDA-MB-231 and BRCA-mut MDA-MB-436 cells (Fig. 4J-M and Fig. S4F). Conversely, overexpressing ACIL in MDA-MB-231, Hs578T and MCF-7 cells increased Chk1 phosphorylation induced by ADM (Fig. 4N–S and Fig. S4G).

To further confirm whether ACIL regulated Chk1 phosphorylation in other types of cancer cells, we examined HNE1 nasopharyngeal carcinoma cells and H1299 non-small cell lung cancer cells. Knockdown of ACIL reduced the phosphorylation level of Chk1 in these two cell lines post ionizing radiation (IR), and did not interfere with the activation of the ATM-Chk2 pathway (Figs. S4H–K). Thus, ACIL regulates the DNA damage response of multiple tumor types by interacting with Chk1 and enhancing its phosphorylation.

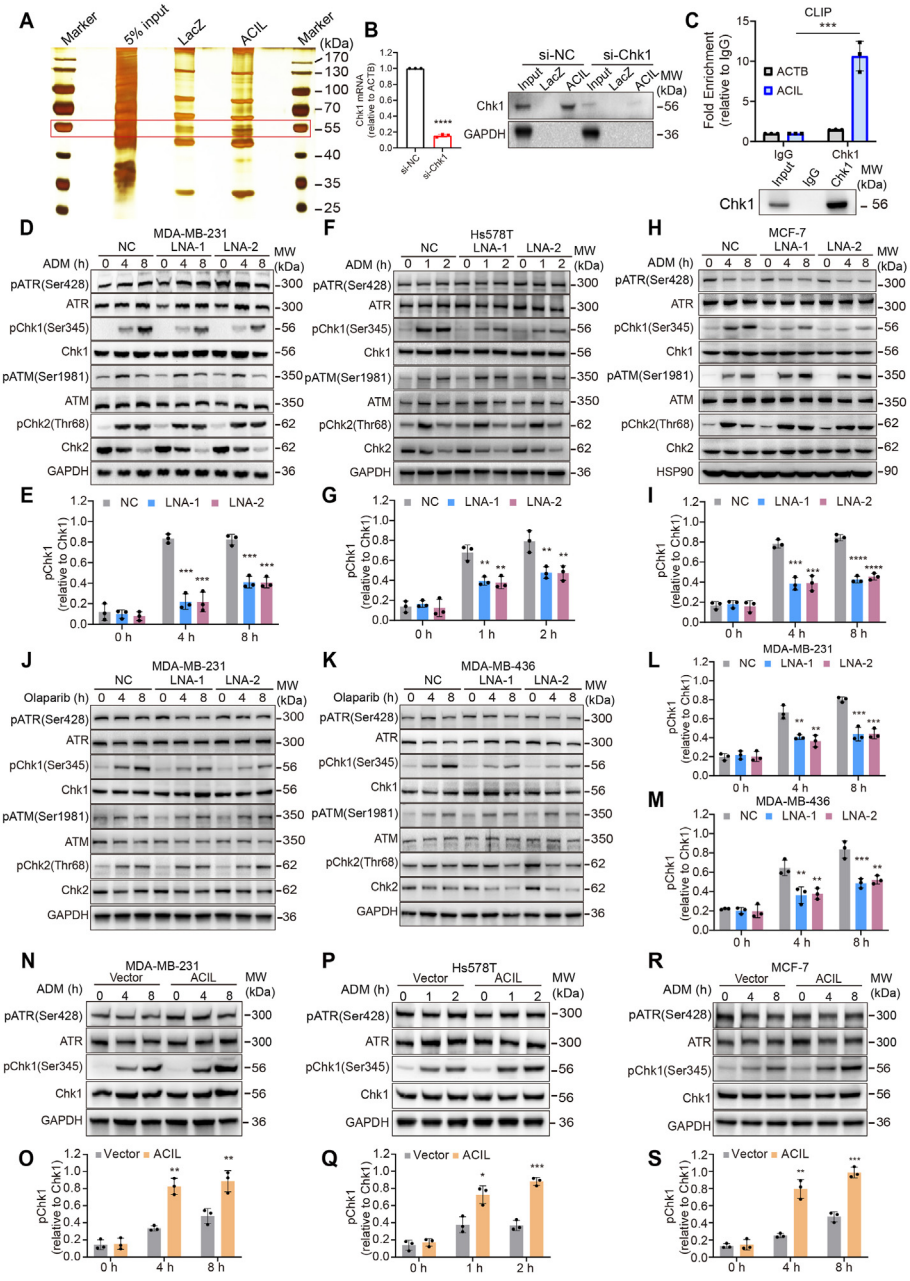

Fig. 4. ACIL interacts with Chk1 and promotes its phosphorylation. (A) Silver staining of proteins binding to LacZ mRNA or ACIL. The gel in red frame is cut for the mass spectrum analysis. (B) RT-qPCR shows the efficacy of siRNA of Chk1 (left). RNA pulldown followed by WB shows binding of Chk1 to ACIL (right). (C) CLIP assay shows that ACIL is enriched about 10-fold in the Chk1 precipitates than in the IgG precipitates. WB verification of Chk1 IP is presented below. (D–I) Protein levels of ATR-Chk1 and ATM-Chk2 pathways in NC- and ACIL-knockdown MDA-MB-231 (D–E), Hs578T (F–G), MCF-7 (H–I) cells after ADM treatment (1 μg/mL). J-M, Protein levels of ATR-Chk1 and ATM-Chk2 pathways in NC- and ACIL-knockdown MDA-MB-231 (J, L) and MDA-MB-436 (K, M) cells after Olaparib treatment (150 mM for MDA-MB-231 cells, 100 mM for MDA-MB-436 cells). (N–S) ACIL overexpression increases ADM-induced Chk1 phosphorylation in MDA-MB 231 (N–O), Hs578T (P–Q) and MCF-7 (R–S) cells. Quantifications of phosphorylated protein relative to total protein are shown in (E, G, I, L, M, O, Q, S). The result is presented as mean ± SD of experimental triplicates (B, C, E, G, I, L, M, O, Q, S), and *P* value was assessed by two-tailed unpaired *t*-test (B–C) and one-way ANOVA with Dunnett's multiple comparisons test (E, G, I, L, M, O, Q, S). *, $P < 0.05$; **, $P < 0.01$; ***, $P < 0.001$; ****, $P < 0.0001$.

2.5. *ACIL promotes Chk1 phosphorylation by ATR*

To investigate whether ACIL promoted ATR phosphorylation or suppressed pChk1 dephosphorylation, we compared ACIL binding capacity to Chk1 and pChk1. The CLIP assay revealed that ACIL was most abundantly enriched in Chk1 immunoprecipitates, and appreciably enriched in ATR immunoprecipitates, but not in pChk1 immunoprecipitates when compared to IgG (Fig. 5A). To validate this observation, we pretreated cell lysates with phosphatase before performing RIP assays. The enrichment of ACIL could still be detected in both Chk1 and ATR immunoprecipitates (Fig. 5B), indicating that ACIL might link Chk1 to its kinase ATR.

To investigate whether ACIL facilitate Chk1 phosphorylation by ATR, we performed the *in vitro* kinase assay in MDA-MB-231 cells. When exposed to ADM, Chk1 could be phosphorylated by the activated ATR at S345, and the phosphorylation efficiency of ATR towards Chk1 significantly enhanced in the presence of ACIL, but not the negative control LacZ mRNA (Fig. 5C and D). As ATR inhibitor (ATRi) VE-822 could suppress ACIL overexpression-increased Chk1 phosphorylation (Fig. S5A), we perform the kinase assay in ATRi treated MDA-MB-231 cells, and found ATRi abolished the elevation of Chk1 phosphorylation (Fig. 5C and D). Moreover, RNA FISH followed by immunofluorescence showed the colocalization of ACIL with pATR and Chk1 in the nucleus of MDA-MB-231 cells treated with ADM (Fig. S5B). These results indicate that ACIL facilitates the phosphorylation of Chk1 by ATR.

To explore whether ACIL affect the recruitment of ATR, ATRIP and its activator protein TopBP1 (Lee et al., 2007), we performed chromatin-fraction isolation assay (Wu et al., 2022) in hydroxyurea (HU)-induced DNA damage condition. The Western blot of chromatin fraction showed that ACIL did not affect the recruitment of ATR activator to the chromatin (Fig. S5C). Moreover, ACIL knockdown did not affect the phosphorylation of RPA2 at S33 in MDA-MB-231 and Hs578T cells (Figs. S5D and E), which is a ssDNA binding protein crucial for DNA replication and DNA repair (Vassin et al., 2009), and another substrate of

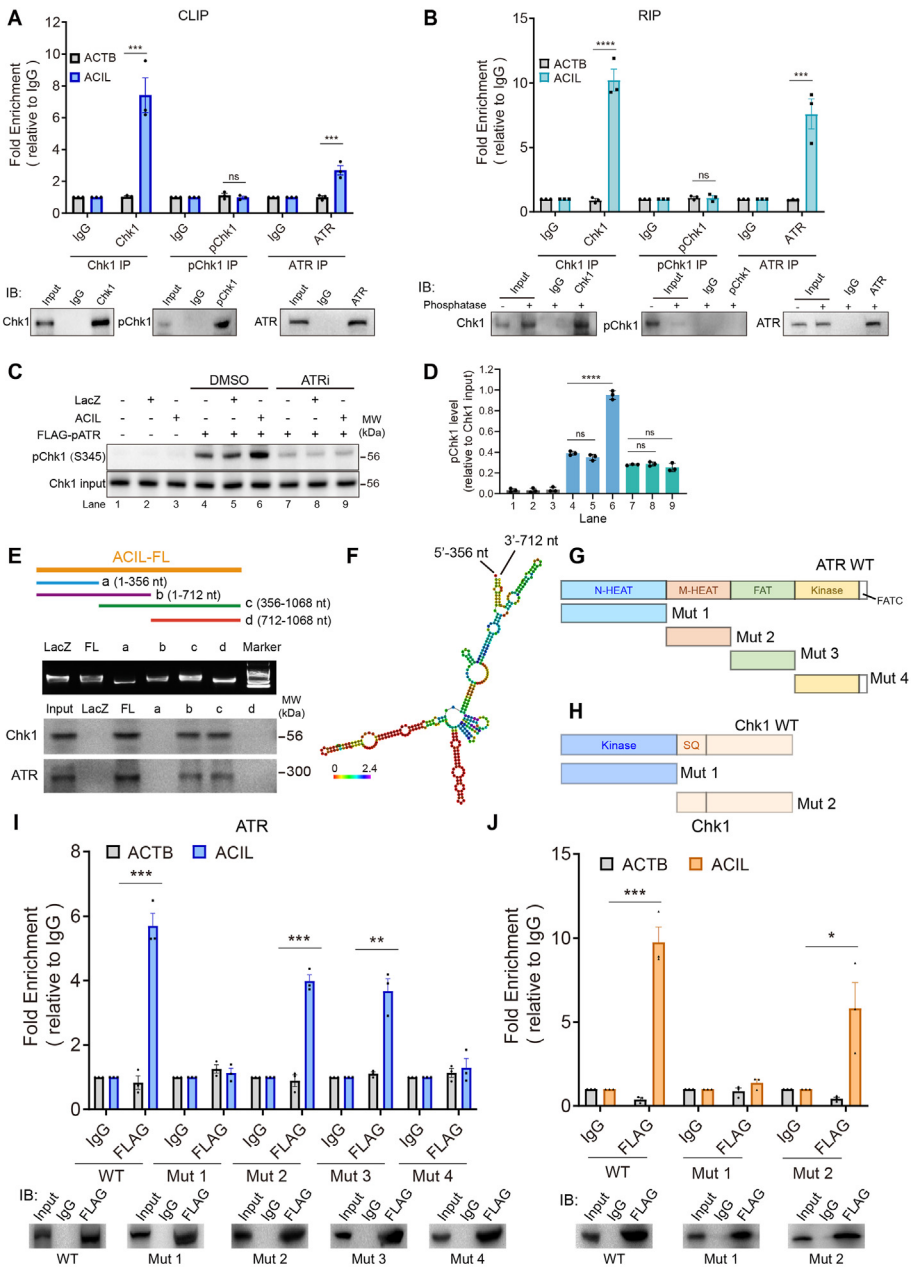

Fig. 5. ACIL enhances the phosphorylation of Chk1 by ATR. (A) CLIP assay shows the enrichment of ACIL by Chk1, pChk1 and ATR antibodies. (B) RIP assay post phosphatase treatment (37 °C for 1 h) shows the enrichment of ACIL by Chk1 and ATR antibodies. (C–D) WB followed by *in vitro* kinase assay shows that ACIL enhances Chk1 phosphorylation induced by FLAG-pATR after ADM (1 μg/mL for 4 h) or ADM combining with ATRi (10 nM for 4 h) exposure in MDA-MB-231 cells lysis (D). Quantification of phosphorylated Chk1 relative to Chk1 input is shown in (D). (E) 356–712 nt of ACIL binds to Chk1 and ATR, as assayed by WB after RNA pulldown. (F) Schematic diagram of the secondary structure of ACIL 356–712 nt. (G–H) Schematic diagrams of full-length or truncated ATR (G) and Chk1 (H) constructs. (I–J) RIP followed by RT-qPCR shows the binding of ACIL to ATR Mut 2 and Mut 3 (I, 1100–2100 aa), as well as to Chk1 Mut 2 (J, 265 to 476 aa). The results are presented as mean ± SEM (A, B, I, J) or SD (D) of experimental triplicates, and *P* value was assessed by two-tailed unpaired *t*-test (A, B, D, I, J). *, $P < 0.05$; **, $P < 0.01$; ***, $P < 0.001$; ****, $P < 0.0001$.

ATR (Olson et al., 2006). The mediator protein Claspin has been reported to in facilitate Chk1 phosphorylation by ATR (Smits et al., 2019). Co-Immunoprecipitation (Co-IP) assay demonstrated that knocking down ACIL impaired the association between Chk1 and ATR, but did not alter the interaction between Chk1 and Claspin when exposed to HU (Fig. S5F). These findings suggest that ACIL acts as a specific scaffold for ATR-Chk1 interaction, and does not impact ATR recruitment, ATR kinase activity towards other substrates or Chk1 interaction with the mediator protein Claspin.

We then constructed a series of truncated mutants to determine the nucleotide sequence of ACIL that bound to Chk1 and ATR (Fig. 5E and Table S3). RNA pulldown assay in MDA-MB-231 cells revealed that nucleotides 356 to 712 in ACIL had comparable capacity with the full-length ACIL in binding to both Chk1 and ATR (Fig. 5E). As there are adjacent stem-loops within nucleotides 356 to 712 of ACIL, according to RNA fold software (Liu et al., 2021), these stem-loops may be the structures responsible for the binding of ACIL to ATR and Chk1 (Fig. 5F). To identify the domains of ATR and Chk1 that interact with ACIL, we also generated the series of truncated ATR and Chk1 constructs (Fig. 5G and H, Tables S4 and 5). RIP assays in HEK 293 cells showed that the M-HEAT and FAT domains of ATR (residues 1100 to 2100 aa) and the C-termini of Chk1 (residues 265 to 476 aa) had relatively higher binding capacities with ACIL, respectively (Fig. 5I and J, Figs. S5G and H). These data suggested that ACIL might serve as a molecular scaffold between ATR and Chk1 by virtue of two adjacent stem-loops, so as to enhance the phosphorylation of Chk1 by ATR.

2.6. *ACIL regulates ATR-Chk1 pathway in the response to DNA damage*

Cell cycle checkpoint is a critical protection system for DNA damage and replication stress in normal and tumor cells. Activation of the ATR-Chk1 pathway upon DNA damage will induces cell cycle arrest, stabilizes replication forks, and regulates HR repair, whereas the failure of ATR-Chk1 activation results in the malfunction of these processes (Gupta et al., 2022). Flow cytometry analysis of EdU staining showed that silencing ACIL significantly compromised the S phase arrest in

MDA-MB-231 and MCF-7 cells after CDDP treatment (Figs. S6A–D). These results were similar with that inhibition of ATR-mediated phosphorylation of Chk1 impeded S phase arrest upon DNA damage (Zhang & Hunter, 2014). Moreover, when treated with HU, an inhibitor of DNA replication that could induce replication stress (Petermann et al., 2010), ACIL-knockdown MDA-MB-231 and MCF-7 cells exhibited severely compromised S phase arrest compared to negative control cells (Figs. S6E–H). Thus, ACIL induce cell cycle checkpoint arrest upon DNA damage and replication stress.

Activation of ATR in response to DNA damage stalls the replication fork and reduces origin firing in S phase, thus allowing DNA damage repair (Saldivar et al., 2017). Inhibition of ATR or Chk1 decreases replication fork stability, slows replication fork progression, and leads to unscheduled origin firing. To evaluate whether ACIL involved in ATR-Chk1-regulated replication fork stability, we performed the DNA fiber assay using HU treatment (Okamoto et al., 2021). A shorter length of replication fork prolongation was observed in ACIL-knockdown MDA-MB-231 cells as compared to NC-knockdown cells after exposure to HU (Fig. 6A and Fig. S6I). Moreover, the speed of replication fork prolongation was significantly suppressed in ACIL knockdown cells upon HU exposure (Fig. 6B). Under replication stress, the replication fork exhibited three different states, namely new origin, ongoing fork and stalled fork (Fig. S6J). In ACIL knockdown cells, there was a dramatic increase in the proportion of new origin forks, and the proportion of stalled forks decreased, indicating the explosion of unscheduled new origin firing in these cells (Fig. 6C and D). On the other hand, ACIL-overexpressed MDA-MB-231 cells exhibited a longer length and a higher speed of replication fork prolongation in the presence of HU (Fig. 6E and F, Fig. S6K). Furthermore, the proportion of ongoing fork that representing stable forks increased in MDA-MB-231 cells with ACIL overexpression under HU treatment (Fig. 6G and Fig. S6L). These results suggested that ACIL played a vital role in replication stress response via regulating replication fork stability and origin firing.

Replication protein A (RPA), composed of RPA1, RPA2, and RPA3, safeguards the DNA template chain during replication and DNA damage repair and preserves ssDNA integrity (Maréchal & Zou, 2015; Zou & Elledge, 2003). The RPA-ssDNA complex is critical structure for activation of ATR signaling, which could be specifically detected by RPA2 foci immunofluorescence (Zeman & Cimprich, 2014). However, the exhaustion of RPA leads the replication fork collapse, and converting to severe

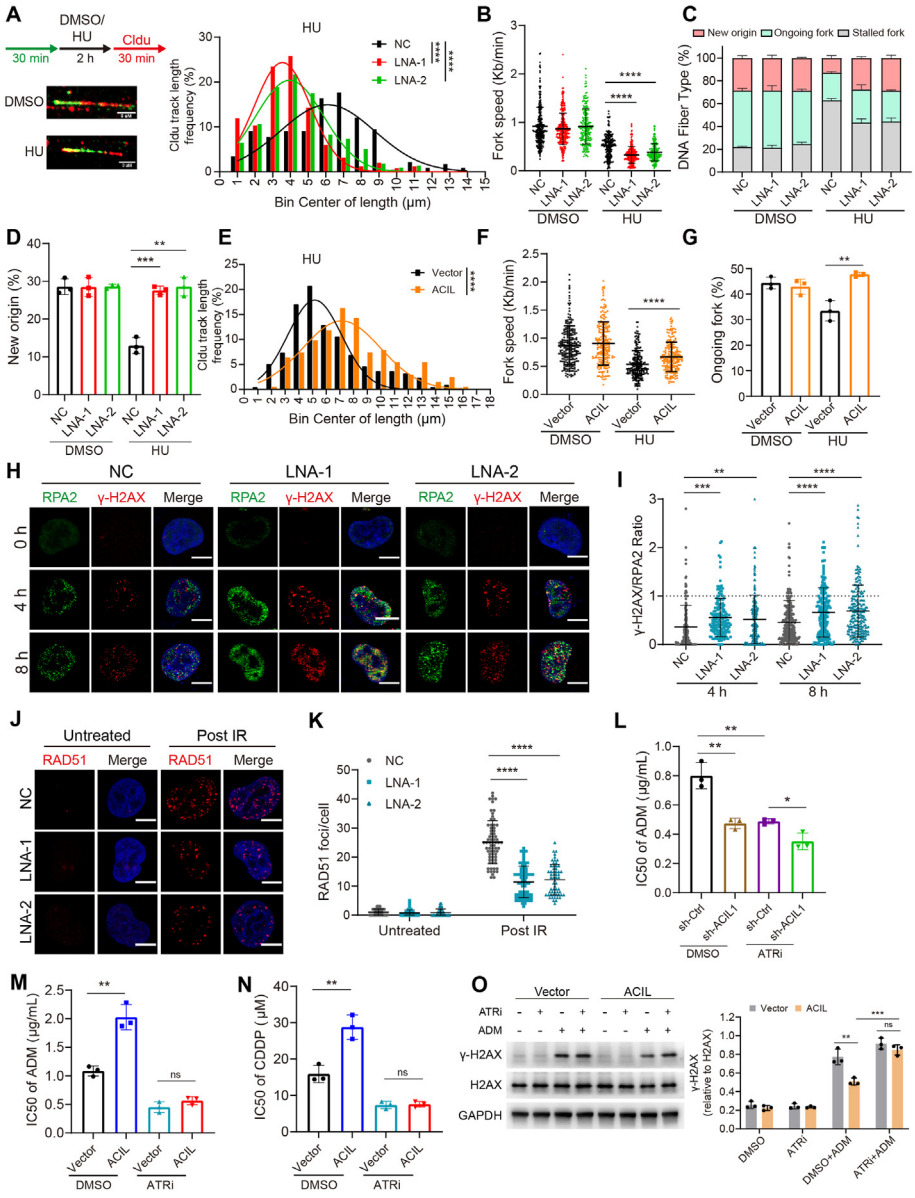

Fig. 6. ACIL protects cancer cells from replication stress and DNA damage through ATR-Chk1 pathway. (A) ACIL knockdown reduces Cldu track length after HU exposure in MDA-MB-231 cells. Schematic diagram and representative images of DNA fiber assay (left) upon DMSO or HU exposure (0.5 mM for 2 h). The distribution of fork progression length by the nonlinear Gaussian fitting of represented data is shown (right). Scale bar = 3 μm. (B) Statistical graph of fork speed shows knockdown of ACIL impairs the replication fork stability in (A). A conversion with the equation of 1 μm = 2.59 Kb. (C) The distribution quantification of replication fork types. (D) Knockdown of ACIL increases the proportion of the new origin fork. (E) The distribution of fork progression length in MDA-MB-231 cells after HU exposure. The represented data is presented as Nonlinear Gaussian fitting. (F) Statistical graph of fork speed shows that overexpression of ACIL protects the replication fork stability in (E). Conversion with the equation of 1 μm = 2.59 Kb. (G) The distribution quantification shows overexpression of ACIL increases the proportion of ongoing forks. (H) Representative images of RPA2 and γ-H2AX foci formation after HU exposure (1 mM for 0, 4, 8 h) in MDA-MB-231 cells. Scale bar = 10 μm. (I) Quantifications of γ-H2AX and RPA2 foci number ratio in (H). (J) Representative images of RAD51 foci formation post IR or not (10 Gy, repair for 2 h) in MDA-MB-231 cells. Scale bar = 10 μm. (K) Quantifications of RAD51 foci number in (J). (L) IC50 of ADM in ACIL stably knockdown MDA-MB-231 cell in combination with ATRi (10 nM). (M–N) IC50 of ADM (M) and CDDP (N) in ACIL overexpressed MDA-MB-231 cell in combination with ATRi (10 nM). (O) Overexpression of ACIL decreases ADM (1 μg/mL for 4 h)-induced γ-H2AX level in MDA-MB 231, while the level of γ-H2AX is reversed when combined with ATRi (1 nM). The results are presented as mean ± SD, and *P* value was assessed by one-way ANOVA with Dunnett's multiple comparisons test (B, D, I, K, L-N), two-tailed unpaired *t*-test (F, G, O). *, $P < 0.05$; **, $P < 0.01$; ***, $P < 0.001$; ****, $P < 0.0001$.

DSBs (Sirbu et al., 2011; Toledo et al., 2013). Our findings suggested that ACIL knockdown triggered the explosion of unscheduled new origin firing (Fig. 6C and D), which may cause the excessively recruitment and exhaustion of RPA. Subsequently, we investigated the generation of DSBs in HU-induced replication stress. As shown by immunostaining, RPA2 foci gradually accumulated in control MDA-MB-231 cells when exposed to HU, some of which converted to severer DNA damages, as detected by γ-H2AX foci formation (Fig. 6H and I). Notably, more RPA2 foci accumulation, as well as severer DNA damage were detected in ACIL-knockdown MDA-MB-231 cells (Fig. 6H and I). Moreover, unrepair DNA damage is a well-known source of replication stress (Zeman & Cimprich, 2014). We examined the RPA2 foci accumulation after UV exposure, which induced ssDNA damage either directly or indirectly. ACIL knockdown increased the RPA2 foci accumulation after UV exposure, indicating an excessive sequester of RPA upon SSB in ACIL-knockdown MCF-7 cells (Fig. S6M). These results were reminiscent of ATR inhibition that caused RPA pool exhaustion, leading to replication fork collapse and double-strand DNA breakage (Toledo et al., 2013).

In addition, we examined whether ACIL affected the role of ATR-Chk1 in contributing to HR repair (Zhao et al., 2019). After IR, fewer RAD51 foci was observed in ACIL-knockdown MDA-MB-231 cells (Fig. 6J and K), indicating that knockdown of ACIL reduced HR repair in DSBs. Together, ACIL protects cancer cells against DNA damage by inducing cell cycle arrest, stabilizing replication forks and prohibiting replication catastrophe, as well as contributing to the HR repair.

To validate that ACIL acts through the ATR-Chk1 pathway, we treated stable ACIL-knockdown cells with ATRi. The IC50 of ADM was significantly decreased in sh-ACIL1 knockdown or ATRi treated MDA-MB-231 cells. However, ATRi treatment in ACIL-knockdown cells could only slightly decrease the IC50 of ADM (Fig. 6L and Fig. S6N-O), indicating that sh-ACIL1 knockdown and ATRi might act through the same pathway. We revisited major phenotypes of overexpressing ACIL and tested whether ATR inhibitors abrogated these phenotypes. The cell viability assay revealed that lentivirus-mediated ACIL-overexpressed MDA-MB-231 cells exhibited resistance to ADM compared to the control cells, while the ADM IC50 decreased dramatically when combined with

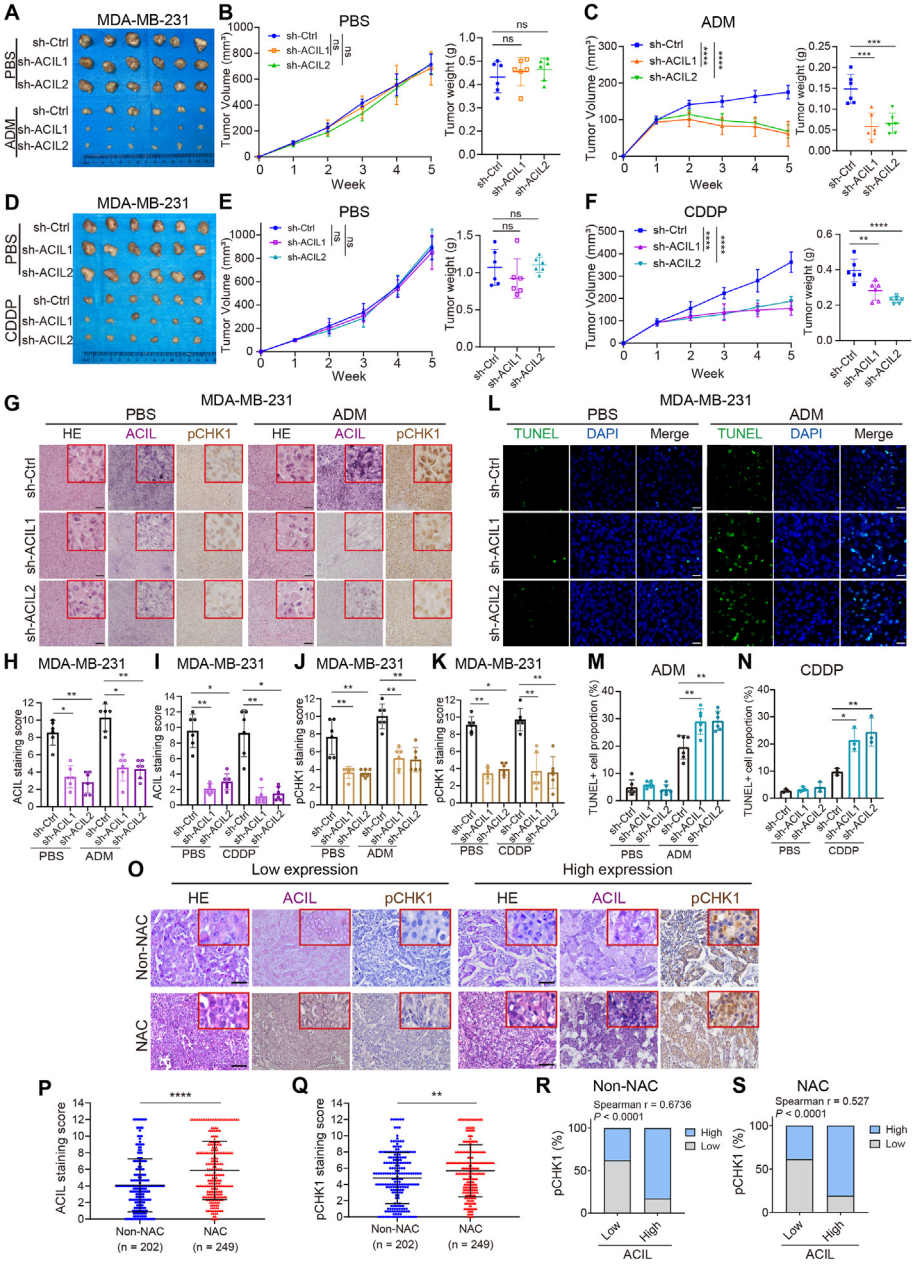

Fig. 7. Knockdown of ACIL sensitizes breast cancer to chemotherapies *in vivo*. (A) ACIL knockdown sensitizes MDA-MB-231 xenografts to ADM treatment. Stable Ctrl- and ACIL-knockdown MDA-MB-231 cells were injected into mammary fat pads of nude mice. PBS or ADM (5 mg/kg) were injected intraperitoneally once a week. (B–C) The tumor growth curves and tumor weights in (A). (D) ACIL knockdown sensitizes MDA-MB-231 xenografts to CDDP treatment. PBS or CDDP (5 mg/kg) were injected intraperitoneally twice a week. (E–F) The tumor growth curves and tumor weights in (D). (G) Representative images of HE staining, ACIL ISH and pChk1 IHC in xenograft sections. Scale bar = 100 μm. (H–I) Statistical graph of ACIL ISH staining score in tumor sections. (J–K) Statistical graph of pChk1 IHC staining score in tumor sections. (L) Representative images of TUNEL assay in MDA-MB-231 xenografts. Scale bar = 20 μm. (M–N) Quantifications of TUNEL-positive cells in xenografts. (O) Representative images of HE staining, ACIL ISH and pChk1 IHC in human breast cancer tissues with or without NAC treatment. Scale bar = 400 μm. (P–Q) Both ACIL (P) and pChk1 (Q) levels are higher in NAC breast cancer tissues than in non-NAC tissues. Data are shown as mean ± SD. (R–S) The Spearman correlation analysis shows a significantly positive correlation between ACIL and pChk1 in non-NAC breast cancer tissues (R, $n = 202$) and NAC breast cancer tissues (S, $n = 249$). The results are presented as mean ± SD of $n = 6$ (B, C, E, F, H–K, M) or $n = 3$ (N), and P value was assessed by one-way ANOVA with Dunnett's multiple comparisons test (B, C, E, F, M, N), Kruskal-Wallis test (H–K), two-tailed Mann-Whitney test (P, Q), nonparametric Spearman correlation (R, S). *, $P < 0.05$; **, $P < 0.01$; ***, $P < 0.001$; ****, $P < 0.0001$.

ATRi (Fig. 6M and Fig. S6P-Q). Similar results were also obtained in ACIL-overexpressed MDA-MB-231 cells when exposed to CDDP combined with ATRi (Fig. 6N and Fig. S6R). We also detected the level of γ-H2AX after exposure to ADM, which showed that γ-H2AX level decreased in ACIL-overexpressed MDA-MB-231 cells, but this effect was reversed when treated with ATRi (Fig. 6O). These results suggested that ATR inhibitor specifically counteracted the effect of ACIL in DNA damage response.

2.7. *ACIL knockdown sensitizes breast cancer to chemotherapy in vivo*

To further explore whether ACIL regulates chemoresistance in breast cancer cells *in vivo*, we generated xenografts by orthotopically injecting MDA-MB-231 or MCF-7 cells infected with the lentivirus-mediated expression of ACIL shRNA and control shRNA into nude mice. Knockdown of ACIL alone did not affect tumor growth (Fig. 7A, B, D and E), whereas the volume and weight of sh-ACIL xenografts after ADM or CDDP treatment were significantly smaller than sh-control MDA-MB-231 and MCF-7 xenografts (Fig. 7C and F, Figs. S7A and B). ISH demonstrated that ACIL was efficiently knocked down in xenografts (Fig. 7G–I), and ACIL expression correlated with Chk1 phosphorylation levels in both ADM and CDDP treated tumors (Fig. 7J and K). Immunostaining of Ki-67 confirmed that silencing ACIL did not affect cell proliferation *in vivo* (Figs. S7C–F). TUNEL (terminal deoxynucleotidyl transferase dUTP nick end labeling) assay showed that knockdown of ACIL induced more apoptosis in xenografts treated with ADM or CDDP (Fig. 7L-N and Figs. S7G–I). Thus, silencing ACIL enhanced the chemosensitivity of breast cancer *in vivo*.

To confirm the correlation between ACIL and pChk1 expression in human breast cancer, we performed ISH and IHC to examine their expression levels in tumor tissues from in-house breast cancer patients (Fig. 7O). We also compared ACIL and pChk1 levels in breast cancer tissues with or without NAC, and found that ACIL and pChk1 levels increased consistently after NAC treatment in breast cancer patients (Fig. 7P and Q). In both NAC ($n = 202$) and non-NAC ($n = 249$) breast cancer tissues, ACIL expression was positively associated with the level of Chk1 phosphorylation (Fig. 7R and S). These data suggest that ACIL expression is tightly linked with Chk1 phosphorylation in breast cancer patients.

3. Discussion

DDR represents an evolutionarily conserved mechanism that maintains genome integrity (Gaillard et al., 2015). Disrupting the DDR pathways to increase chemosensitivity of cancer cells has been explored as combination treatment strategies in pre-clinical studies (Pilié et al., 2019). Here, we demonstrate lncRNA ACIL as a potential target to overcome chemotherapy resistance in breast cancer. We discover that ACIL highly expresses in chemoresistant breast cancer tissues and is associated with poor patient prognosis. Notably, ACIL promotes the activation of ATR-Chk1 signaling pathway by facilitating ATR and Chk1 interaction. When DNA damage or replication stress occur, high level of ACIL induces cell cycle arrest and stabilizes the replication fork, therefore prolonging the time necessary for DNA repair in cancer cells (Fig. 8). Targeting ACIL induces irreparable DNA damage and enhances the efficacy of anti-tumor DNA damaging agents both *in vitro* and *in vivo*.

Our results reveal that as a novel noncoding regulator of ATR-Chk1 signaling, ACIL acts in cell cycle checkpoint, replication fork stability and DNA repair. First, ACIL regulates the S phase arrest in DDR. Our findings demonstrate that knockdown of ACIL in breast cancer cells results in reduced intra-S phase arrest after exposure to CDDP and HU, indicating ACIL acts in the S-G2 phase checkpoint of breast cancer cells. Second, ACIL stabilizes replication forks. The high expression of ACIL stalls and stabilizes the replication forks in S phase, which maximumly protects replication forks from collapse after DNA damage. The knockdown of ACIL causes the unscheduled origin firing upon replication stress, which has been reported to excessively exhaust the RPA pool, induce the replication fork to collapse and further convert to the lethal DSB (Toledo et al., 2013). Third, ACIL participates in HR repair. Silencing ACIL reduces the RAD51 focus formation and impairs the HR repair of DNA damage. As the downstream substrate of ATR, Chk1 promotes the expression and activation of RAD51 and regulates the distribution of RAD51 to DNA damage sites (Gupta et al., 2022). The above lines of evidence suggest that ACIL orchestrates the response to replication stress

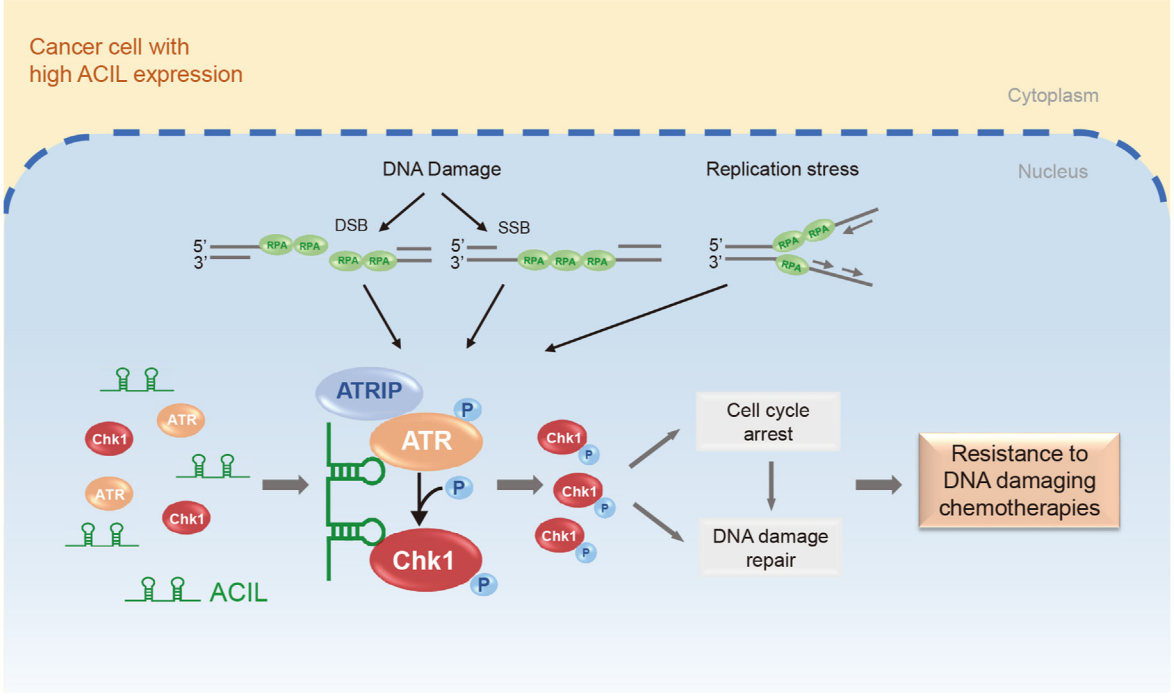

Fig. 8. Schematic illustration of ACIL in regulating the ATR-Chk1 pathway to promote chemoresistance of breast cancer cells.

and DNA damage, which is analogous to the function of ATR-Chk1 signaling pathway.

In our *in vitro* study, ACIL knockdown using LNAs did not affect the proliferation of MDA-MB-231 and MCF-7 cells (Figs. S2B–E). Our animal experiments further revealed that ACIL did not influence the growth of MDA-MB-231 and MCF-7 xenografts in the PBS condition. In consistence, Chk1 siRNAs did not interfere with cell growth in various cell lines under normal conditions, but sensitized cancer cells to chemotherapy agents, such as doxorubicin and 5-FU (Ganzinelli et al., 2008). We think that although tumor cells are subjected to strong endogenous DNA damage, they may have been adapted to these stresses in normal conditions. Thus ACIL, even Chk1, may be dispensable for cell proliferation. However, we noted a significant increase in ACIL expression under treatment of DNA-damaging drugs, suggesting that the role of ACIL is more pronounced when the ATR-Chk1 pathway needs to be extensively activated in response to DNA damage.

The activation of Chk1 by ATR requires mediator proteins (Yazinski & Zou, 2016), among which Claspin specifically tethers ATR and Chk1 together to mediate Chk1 phosphorylation by ATR (Hsiao et al., 2021; Smits et al., 2019). Our study uncovers that ACIL directly binds to ATR at the M-HEAT and FAT domains and Chk1 at the C-terminal. It has been reported that the M-HEAT and FAT domains of ATR harbor protein binding site and may pose an auxiliary effect on the kinase activity of ATR (Rao et al., 2018). The C-termini of Chk1 contains a serine/glutamine-rich region with multiple ATR phosphorylation sites (Zhang & Hunter, 2014). These results suggest ACIL plays a mediator role in ATR-Chk1 signaling pathway. Different from Claspin (Bianco et al., 2019; Yang et al., 2016), ACIL exerts minimal impact on the cell cycle distribution and cell viability in the absence of drug-induced DNA damage in our study. Moreover, ACIL modulates ATR-Chk1 signaling pathway at a post-transcriptional level in an ATR-dependent manner. To our knowledge, ACIL is the first reported RNA adaptor that connects ATR and Chk1 and promotes the activation of this signaling pathway.

Different chemotherapeutic agents cause various types of DNA damages. Adriamycin, for example, can trap topoisomerase II (TOP2) and cause irreversible TOP2-linked DNA double-strand breaks (Canela et al., 2019), while platinum compounds and alkylating agents, such as cisplatin and cyclophosphamide, form bulky drug-DNA adducts, induce DNA base lesions and inter-strand or intra-strand cross-links (Bruno et al., 2017; Crook et al., 1986). It has been proposed that the ATR-Chk1 signaling pathway is activated by ssDNA that is exposed from the single-strand break and replication stress (Simoneau & Zou, 2021), the free ssDNA ends in dsDNA damage and the ssDNA ends generated in the process of HR repair (Costanzo et al., 2003; Sartori et al., 2007; Shiotani & Zou, 2009). In our study, we used different DNA damaging agents and found that ACIL expression induces resistance of breast cancer to all these DNA damaging chemotherapy drugs as well as PARP inhibitors. As ACIL knockdown reduces the level of phosphorylated Chk1 upon treatment of DNA damaging agents, and inhibition of ATR abrogates the drug resistance induced by ACIL overexpression, we reason that the effect of ACIL is attributed to the enhanced activation of ATR-Chk1 pathway which avoids aggravating DNA damage and promotes DNA repair.

Previous research has reported diverse functions of LRRC75A-AS1. In triple-negative breast cancer (TNBC), LRRC75A-AS1 enhances the expression of the oncogene BAALC by suppressing miR-380-3p, revealing the regulatory role of LRRC75A-AS1 through a ceRNA network in TNBC cells (Li et al., 2020). Similarly, LRRC75A-AS1 antagonizes the downregulation effect of miR-223-3P on CTNND1 expression, suggesting LRRC75A-AS1 promotes the progression of glioblastoma (Han et al., 2019). Moreover, LRRC75A-AS1 promotes the upregulation of PD-L1 expression by enhancing the stability of YAP protein, thereby inhibiting the anti-tumor immunity in colorectal cancer (Ni et al., 2021). Our findings demonstrate LRRC75A-AS1 contributes to chemoresistance in breast cancer via regulating ATR-Chk1 signaling pathway. This highlights a novel approach to enhance chemosensitivity of breast cancer by targeting LRRC-75A-AS1.

The application of RNA therapies has shown tremendous potential in anti-cancer therapy (Nguyen & Than, 2024). In our study, the high expression of ACIL in chemoresistant breast cancer tissue may be a biomarker for predicting the sensitivity to DNA-damaging drugs, as well as a potential target for combination therapy with chemotherapy. Targeting may provide a more specific and potent strategy for chemoresistant cancer cells and minimizing the impact on normal cells. Knocking down ACIL can be achieved through techniques like LNA-modified ASO, as demonstrated in our study. Although targeting noncoding RNA remains challenging in clinic (Winkle et al., 2021), with technical advancements, promising emerging approaches will improve the efficacy, specificity and delivery of RNA-based therapeutics.

Together, our work reveals the role of ACIL in inducing resistance to DNA damaging agents in breast cancer. Targeting ACIL in combination with chemotherapy may provide additional options for patients who have de novo or acquired chemoresistance. As a specific regulator of the ATR-Chk1 signaling pathway, ACIL has the potential to be not only a biomarker for chemoresistance but also a therapeutic target in breast cancer.

4. Material and methods

4.1. Patients and tissue samples

Formalin-fixed and paraffin-embedded tissues (non-NAC $n = 202$, NAC $n = 298$) and fresh tumor tissues ($n = 80$) were obtained from breast cancer patients of Sun Yat-Sen Memorial Hospital, Sun Yat-Sen University. All samples were collected with signed informed consent from the patients according to Sun Yat-Sen Memorial Hospital's internal review and ethics board (project number SYSEC-KY-KS-2023-171).

4.2. Cell lines and cell culture

MDA-MB-231, Hs578T, MDA-MB-468, MDA-MB-436, MCF-7, H1299, HEK 293, and MCF-10A cell lines were purchased from the American Type Culture Collection (ATCC). HNE1 cell line was generously provided by Dr. Musheng Zeng from the Sun Yat-Sen University Cancer Center. The cell lines were cultured in DMEM medium (Gibco) supplemented with 10% fetal bovine serum (Gibco) and maintained in a humidified incubator at 37 °C and 5% CO2. To induce CDDP-resistant cells, a low initial concentration (1 μM) of CDDP with gradual increments was used in MDA-MB-231 cells over a 7-month period. The sensitivity to CDDP of MDA-MB-231 cells was detected using the CellTiter-Glo Luminescent Cell Viability Assay Kit (#G7572, Promega). Chemotherapy drugs adriamycin (doxorubicin, #E2516), cisplatin (#S1166), hydroxyurea (#S1896), and cyclophosphamide (#S1217), ATR inhibitor (VE-822, #S7102) were purchased from Selleck. The detailed concentration of chemotherapy drugs were listed in the results and figure legends.

4.3. RNA extraction and quantitative real-time PCR

Total RNA was extracted from cultured cells using TRIzol (#MAN0001271, Invitrogen) in a 1.5 mL RNase-free tube according to the manufacturer's protocol. Briefly, 1 mL TRIzol was added to lyse 50 mg tissue or 1 × 105–107 cells, followed by a 5-min incubation at room temperature. Added 0.2 mL chloroform (#67663, GHTECH) to TRIzol lysate and mixed thoroughly by shaking, incubated for 3 min, 12000 g centrifugation for 15 min at 4 °C to get an aqueous phase. 1:1 (volume) added isopropanol (#67630, GHTECH) to the aqueous phase and incubated for 10 min at room temperature. The RNA pellet was acquired with 12000 g centrifugation for 10 min at 4 °C, washed the RNA pellet with 75% ethanol. The yield and quality of RNA were examined by NanoDrop One (Thermo). 1 μg total RNA was reverse transcribed into first strand cDNAs using the PrimeScript RT reagent Kit (#RR037A, TAKARA). Quantitative real-time PCR (RT-qPCR) was performed using the SYBR Premix Ex *Taq*II kit (#RR820A, TAKARA) on LightCycler 480 System

(Roche). All primer sequences were listed in Supplemental Table S6. For copy number counts, the gradient concentration of pcDNA3.1 vector inserted with full-length ACIL (molecular weight was estimated as 4.29 × 106 g/mol) was used as cDNA plates to make a standard curve, and one cell was calculated as 20 pg RNA.

4.4. Fluorescence in situ hybridization and in situ hybridization

The location of ACIL expression in MDA-MB-231 and MCF-7 cells was detected with fluorescent in situ hybridization (FISH). FISH of ACIL was performed using the digoxin-conjugated oligodeoxynucleotide probes (5′-DiG-ATGATGGCAAGGGACAAAGCTA-3′, customized by Exiqon) according to the manufacturer's protocol. In brief, cells were fixed in 4% formaldehyde and permeabilized in DEPC-treated PBS containing 0.5% Triton X-100, hybridized with 25 nM ACIL probe in the hybridization solution (#AR0152, Boster) overnight at 52 °C. The next day, cells were washed extensively with the solution containing 50% deionized formamide and incubated with the anti-digoxin fluorescein-conjugated antibody (#11207741910, Roche) overnight at 4 °C. The cells were counterstained with DAPI and mounted with the anti-fade mounting medium (#P0126, Beyotime), then imaged using a confocal laser-scanning microscope (TCS-SP5, Leica) with a core data acquisition system (LAS AF Lite, Leica).

For in situ hybridization (ISH), sections of FFPE samples were dehydrated and re-hydrophilization, acidized with 0.2 N HCl for 5 min at 37 °C, washed in DEPC-treated PBS, digested with 0.05% Trypsin (#ZLI-9010, Boster), preincubated in pre-hybrid solution for 2 h and hybridized with 25 nM probe overnight at 52 °C. The tissue was washed extensively, incubated with anti-digoxin monoclonal antibody (#BM0040, Boster) overnight at 4 °C, followed by conjugation with Streptavidin and incubated in BCIP/NBT Alkaline Phosphatase staining solution (#C3206, Beyotime). The sections were mounted and taken pictures under a 20 × objective (Eclipse Ni-E, Nikon). Staining scores were calculated with staining intensity × proportion of positively stained cells (The staining intensity scaled as 0 = no staining, 1 = light ACIL staining, 2 = moderate ACIL staining, and 3 = dark ACIL staining. The proportion of positively stained cells scale was graded as 0, no positive cells; 1, <25%; 2, 25%–50%; 3, 50%–75%; and 4, >75%).

For survival analysis, a staining score of 4 was utilized as the cut-off value, with staining scores ≤4 defined as low level of ACIL and scores >4 as high level. The Kaplan-Meier curves with the Log-rank tests were used to analyze overall survival in breast cancer patients with low and high expression levels of ACIL.

4.5. Rapid amplification of cDNA ends (RACE)

According to the SMARTer RACE 5'/3′ Kit (#634859, Clontech) manufacturer's instructions, the 5′ and 3′ RACE of ACIL was performed. The RNA template for ACIL was purified from MDA-MB-231 cells, and the primers of RACE were used as follows:

5′-race:
GATTACGCCAAGCTTCAACACTGGGTGTAGAAACATGCTTGCC;

3′-race: GATTACGCCAAGCTTACTTGGCCTGTGCCTTTGGAAGC.

4.6. Transfection and transduction of tumor cells

For knockdown experiments with locked nucleic acids (LNAs) antisense oligonucleotides (Qiagen), cells were transfected using Lipofectamine 2000 (#11668030, Thermo) with a final concentration of 40 nM LNA and transfection reagent according to the manufacturer's instructions. ACIL-specific sequences were 5′-CGCAATCTTAAAGAGG-3' (LNA-1) and 5′-CCAAGACCATCCTTTA-3' (LNA-2), and a validated nontargeting oligonucleotide 5′-AACACGTCTATACGC-3′ was used as a control. The sequence targeted by Chk1 siRNA was 5′-GTGATGGATTGGAGTTCAA-3' (RiboBIO).

For overexpression experiments, full-length and mutants of ACIL cDNA sequences were inserted into the pcDNA3.1 vector (IGEBio company, Guangzhou, China) at the *Bam*HI and *Xho*I sites. The ATR wild-type (aa 1–2644), ATR mut 1 (aa 1–1100), ATR mut 2 (aa 1100–1500), ATR mut 3 (aa 1500–2100), and ATR mut 4 (aa 2100–2644) sequences were cloned into pcDNA3.1 with 3 × FLAG tag. The Chk1 wild-type (aa 1–476), Chk1 (aa 1–289), and Chk1 (aa 265–476) sequences were cloned into pcDNA3.1 with 3 × FLAG tag. 1.5–2 μg plasmid DNA was transfected into cell lines with EZ Cell Transfection Reagent (#AC04L099, LIFE iLAB bio), and the RNA expression level was examined after 48 h of transfection.

For stable knockdown expression, the shRNA duplexes designed against ACIL (LRRC75A-AS1, Gene ID: 125144) with the target sequences (sh-ACIL1: GCAAATTCGTGAAGAATCAGC; sh-ACIL2: GGGTATCATTCATTACATT) and nonspecific sequence as sh-Control synthesized by Genechem Company (Shanghai, China) were incorporated into the GV344 vector. For stable overexpression experiments, the control and ACIL gene sequences were incorporated into the CV146 vector. The lentiviral particles containing vectors were generated using HEK293T cells (Genechem Company, Shanghai, China). MDA-MB-231 and MCF-7 cells were transfected with lentivirus-mediated vector for 24 h, and selected with 1 μg/mL puromycin (#P8833, Sigma-Aldrich) starting 3 days post-transfection.

4.7. Cell viability assay

The CellTiter-Glo Luminescent Cell Viability Assay Kit (#G7572, Promega) was used to quantify cell viability with or without different chemotherapy drugs exposure. Briefly, 1 × 103 NC- or ACIL-knockdown cells for cell growth assay and 3 × 103 NC- or ACIL-knockdown cells for chemotherapy drugs IC50 assay were triplicate seeded onto a 96-well plate. For cell growth assay, cells were harvested at 1–5 days after seeding. For chemotherapy drugs IC50 assay, the cells were treated with different gradient concentrations of chemotherapeutic drugs after 12 h of cell seeding. And the cells were harvested 24 h after drug treatment. At the experiment timepoint, the medium was replaced with 200 μL of liquid containing 100 μL of medium and 100 μL of CellTiter-Glo reagent and mixed contents for 15 min on an orbital shaker, transferred 100 μL the cell lysis to an opaque 96-well plate and recorded luminescence in the luminescent channel (Infinite M Nano, Tecan). The experiments were repeated independently for 3 times. The Cell Counting Kit-8 (CCK-8) regent (#K1018, APEXBIO) was used to evaluate cell viability of LNA-knockdown MCF-10A cells. Briefly, the medium was replaced with 100 μL CCK-8 medium (containing 10 μL of CCK-8 regent and 90 μL of DMEM). Incubated at 37 °C for 1 h and recorded the absorbance at 450 nm wavelength. The experiments were repeated independently for 3 times.

4.8. Alkaline Comet Assay

The comet assay was performed using the Reagent Kit for Single Cell Gel Electrophoresis Assay (#4250-050-K, Trevigen). Briefly, cells were collected and suspended with D-PBS, combined cells at 1 × 105/mL with molten LMAgarose (at 37 °C) at a ratio of 1:10 (volume), and immediately pipette 50 μL onto CometSlide. Placed the slides at 4 °C in dark for 30 min, then immersed slides in 4 °C Lysis Solution for 40min. Immersed the slides in freshly prepared Alkaline Unwinding Solution (NaOH 0.4 g, 200 mM EDTA 250 μL, added dH_2O to 50 mL) for 20 min at room temperature. Then the Alkaline Comet Assay in Alkaline Electrophoresis Solution (NaOH 8 g, 500 mM EDTA (pH = 8) 2 mL, added dH_2O to 1 L) was performed. Dried samples at 37 °C for 30 min, then stained samples with SYBR Green and photographed samples with a fluorescence microscope (20 × , Eclipse Ni-E, Nikon). The fluorescence image pictures were analyzed with CaspLab - Comet Assay Software Project (https://sourceforge.net/projects/casp/).

4.9. Western blot

Western blot (WB) was performed with the Bio-RAD Western Blotting System. Briefly, cells were lysed with RIPA Lysis Buffer (#P0013B, Beyotime) and incubated on ice for 30 min. The protein was extracted by 12000 g centrifugation for 15 min at 4 °C. The concentration of protein was detected by Pierce BCA Protein Assay Kit (#23225, Thermo) and recorded by Infinite M Nano System (Tecan) at 570 nm. Protein samples were loaded to 8%–12% SDS-PAGE gels, and run the samples with 80–120 V for 1 h. Then transferred into 0.22 μm PVDF membrane with 250 mA for 1.5–4 h. Blocked the membrane with 5% BSA in TBST for 1 h on a shaker and incubated with a specific primary antibodies pATR (S428) (1:1000, #178407, Abcam), ATR (1:1000, #13934S, CST), pChk1 (S345) (1:1000, #2348S, CST), Chk1 (1:1000, #32531, Abcam), pATM (S1981) (1:1000, #5883S, CST), ATM (1:1000, #2873S, CST), pChk2 (Thr68) (1:1000, #2197S, CST), Chk2 (1:1000, #6334S, CST), γ-H2AX (1:1000, #2577S, CST), H2AX (1:1000, #7631S, CST), GAPDH (1:10000, #60004-1-Ig, Proteintech), HSP90 (1:10000, #60318-1-Ig, Proteintech), FLAG (1:1000, #F1804, Sigma-Aldrich), TopBP1 (1:1000, # A300-111A, Bethyl), Claspin (1:400, #23206-1-AP, Proteintech), ATRIP (1:1000, #11327-1-AP, Proteintech), Histone-H3 (1:1000, #17168-1-AP, Proteintech) overnight at 4 °C. Washed the membrane with TBST three times, incubated with HRP-conjugated secondary antibody at room temperature for 1 h. Washed the membrane with TBST three times and detected the signal with SuperSignal Western Blot Enhancer (#46640, Thermo) and Chemi XX9 imaging system (SYNGENE). The quantifications of protein gray-values were calculated by ImageJ software.

4.10. Flow cytometric analysis

For cell apoptosis assay, the experiment was performed with Annexin V-FITC/PI apoptosis kit (#AP101, MUTI SCIENCES) according to the manufacturer's instructions. Briefly, 1–3 × 106 cells were stained with Annexin V and PI for 15 min, then detected with CytoFLEX Flow Cytometer on FITC and PE channel (CytoFLEX, Beckman Counter). The data were analyzed by FlowJo software (BD Biosciences).

The Click-iT EdU Alexa Fluor 647 kit (#C10424, Thermo) was used to perform the intra-S phase detection according to the manufacturer's instructions. Briefly, cells were treated with 0.2 mM hydroxyurea (HU) or DMSO for 5 h after 48 h of LNA transfection, incubated with 10 μM EdU for 30 min. After trypsinization and washed once with 1% BSA in PBS, the cells were pelleted by centrifugation. Cells were fixed with 100 μL Click-iT fixative for 15 min at room temperature and protected from light. Washed the cell with 1% BSA in PBS, resuspended the cells with permeabilization reagent, and incubated for 15 min. Added pre-prepared Click-iT reaction cocktail and mixed well, incubated for 30 min at room temperature in dark. Washed the cells with 1% BSA in PBS and stained the cells with 0.5 μg/mL DAPI for 5 min. The cell distribution was detected with CytoFLEX Flow Cytometer on APC and PB450 channels and the data were analyzed by FlowJo software (BD Biosciences).

4.11. Microarray analysis

LncRNA expression of breast cancer tissue was examined with the Arraystar Human LncRNA Microarray v3.0 (KangChen Bio-tech, Shanghai, China). Briefly, RNA was extracted with TRIzol (#MAN0001271, Invitrogen) and purified with RNasey Mini Kit (#74104, Qiagen). The RNA was labeled and amplificated with Quick Amp Labeling Kit (#5190-0442, Agilent), then the product was purified to get the complementary RNA (cRNA). Based on the manufacturer's protocols, the labeled cRNA was performed hybridizing with Agilent Gene Expression Hybridization Kit (#5188–5242, Agilent). The data were scanned with Agilent Microarray Scanner and processed with Agilent Feature Extraction Software (Agilent). Fold change more than 5 and false discovery rate less than 0.05 were identified as significantly differential expressing lncRNAs. Microarray data are deposited in NCBI Gene Expression Omnibus (GEO) dataset under accession code GSE221222 (composed of GSE221060 and GSE221061).

4.12. RNA immunoprecipitation and crosslinking immunoprecipitation

RNA immunoprecipitation (RIP) was performed with Magna RIP RNA-Binding Protein Immunoprecipitation Kit (#17–700, Millipore). According to the manufacturer's instructions, cells were lysed with RIP lysis buffer containing protease inhibitor cocktail and RNase inhibitor on ice for 30 min, 12000 g centrifugation for 30 min at 4 °C. Collected the supernatant into 1.5 mL RNase-free tubes, quantify protein concentration using the Pierce BCA Protein Assay Kit (#23225, Thermo), and record it with the Infinite M Nano System (Tecan) at 570 nm. Treated cell lysates with FastAP Thermosensitive Alkaline Phosphatase (#EF0651, Thermo) according to the user's guide, incubated at 37 °C for 1 h, and stopped the reaction with a final concentration of 50 mM EDTA (#R1021, Thermo). Divided the lysates into two equal parts in RNase-free tubes on ice. According to the Magna RIP RNA-Binding Protein Immunoprecipitation Kit (#17–700, Millipore) manufacturer's instructions, washed 50 μL magnetic beads per sample, resuspended them with 100 μL of RIP wash buffer, added 5 μg specific antibodies or IgG, and rotated for 1 h at room temperature. Mixed the cell supernatants with beads-antibodies and incubated with rotation overnight at 4 °C. Separated beads and supernatant with the magnetic separator and washed the beads three times with RIP wash buffer. Incubated the samples with 150 μL proteinase K buffer at 55 °C for 30 min. Exacted the RNA with TRIZol LS (#10296028, Thermo) and chloroform, collected the aqueous phase with a new RNase-free tube. 1:1 (volume) added isopropanol and incubated for 10 min. Pelleted RNA by centrifugation and washed with 75% ethanol. Resuspended RNA with 10 μL RNase-free water, then analyzed with reverse transcription-PCR and RT-qPCR.

For UV crosslinking immunoprecipitation (CLIP), the cells were washed with cold PBS and irradiated with UV at 400 mJ/cm2 (254 nM, UVP Hybrilinker Oven, Analytik jena), and lysed with RIP lysis buffer on ice for 30 min. The following protocols were the same as RIP assay performed with Magna RIP RNA-Binding Protein Immunoprecipitation Kit (#17–700, Millipore).

4.13. RNA pulldown

For RNA pulldown, the 3′-end biotin-labeled ACIL was transcribed and labeled with manufacturer's instructions. Briefly, pcDNA3.1-ACIL full-length, ACIL mutants or control-LacZ plasmid were linearized to generate 5′ overhangs. The linear DNA was purified with agarose gel and Gel Extraction Kit (#D2500-02, Omega). According to the user's guide of Transcript Aid T7 High Yield Transcription Kit (#K0441, Thermo), the reaction buffer containing 1 μg template DNA and NTP mix was incubated for 2 h at 37 °C. The RNA product was purified with MEGAclean Kit (#AM1908, Ambion). 50 pmol total RNA was labeled with Pierce RNA 3′ End Desthiobiotinylation Kit (#20163, Thermo) according to the user's guide. 50 μL streptavidin magnetic beads were washed with 20 mM Tris on the magnetic separator and resuspended with RNA Capture Buffer according to the user's guide of Magnetic RNA-Protein Pull-Down Kit (#20164, Thermo). Added 50 pmol folded and labeled RNA into the streptavidin magnetic beads, incubated 30 min at room temperature with rotation. RNA-bound beads were washed with 20 mM Tris and 100 μL Protein-RNA Binding Buffer on the magnetic separator. Lysate of MDA-MB-231 cells was prepared with IP lysis buffer, and the protein concentration was greater than 2 μg/μL. Added the protein lysate to RNA-Protein Binding Reaction buffer and incubated 60 min at 4 °C with rotation. Collected the beads on the magnetic separator and washed them three times with wash buffer. Added 50 μL Elution buffer and incubated 30 min at 37 °C. Then samples were collected for WB or mass spectrometry analysis.

4.14. Mass spectrometry

For mass spectrometry analysis of candidate protein samples, silver staining after the gel electrophoresis was performed according to the manufacturer's protocols with the Pierce Silver Stain for Mass Spectrometry kit (#24600, Thermo). Washed the gel with ultrapure water and fixed the gel with a solution containing 60% water, 30% ethanol, and 10% acetic acid. Washed the gel with 10% ethanol and ultrapure water. Incubated the gel with prepared sensitizer working solution for 1 min and stain working solution for 30 min. Added the developer working solution and incubated for 3 min, then added 5% acetic acid solution to stop the reaction. Collected the interested protein band by destaining and extracting, then analyzed by Guangzhou Fitgene Biotechnology Company.

4.15. In vitro kinase assay

Briefly, FLAG-pATR was purified with FLAG antibody (#F1804, Sigma-Aldrich) and the Dynabeads Protein G (#10004D, Invitrogen) in MDA-MB-231 cells after ADM exposure (1 μg/mL for 4 h) and combining with ATRi (VE-822, 10 nM, 4 h) or DMSO. The kinase reactions were performed in 40 μL of kinase buffer (20 mM Tris-HCl pH = 7.5, 2 mM DTT, 10 mM MgCl2), and contained 200 μM ATP and the substrate containing 2 μg of purified FLAG-pATR protein, 50 ng recombinant human Chk1 protein (#ab69918, Abcam) and 5 pmol purified ACIL RNA at 30 °C for 30 min, placed on ice to stop the reaction. The phosphorylation level of Chk1 (S345) was detected by WB.

4.16. Chromatin-fraction isolation assay

5 × 106 MDA-MB-231 cells were seeded in 10 cm dishes overnight, treated with DMSO (1:1000) or HU (0.5 mM) for 24 h before cells harvested to 1.5 mL microcentrifuge tubes. Ice-cold PBS washed the cells, 130 g centrifugation for 3 min at 4 °C. Gently resuspended cells with Buffer A (containing 10 mM Hepes pH 7.9, 0.34 M sucrose, 20% glycerol, 1 mM dithiothreitol [DTT], 10 mM KCl, 1.5 mM $MgCl_2$, 0.1% Triton X-100, 1 × protease inhibitor cocktail), 1100 g centrifugation for 2 min at 4 °C. Retained pellets and washes the pellets with Buffer A (without 0.1% Triton X-100). Resuspended pellets with Buffer B (containing 30 mM EDTA, 0.2 mM EDTG, 1 mM DTT, 1 × protease inhibitor cocktail), incubated on ice for 10 min, 13000 g centrifugation for 1 min at 4 °C. Collected chromatin pellets and resuspended with Buffer B, measured protein concentration with Pierce BCA Protein Assay Kit (#23225, Thermo) and proceed to Western blot analysis.

4.17. Co-immunoprecipitation (Co-IP) assay

MDA-MB-231 cells were plated into 10 cm dishes overnight, treated with HU (0.5 mM) for 24 h. Before harvesting cells, 0.3% formaldehyde was used for cross-linking for 10 min at room temperature, stopped cross link with glycine in a final concentration of 0.125 M. Cell lysis was performed using Pierce IP lysis buffer (#87788, Thermo) supplemented with 1 × protease inhibitor cocktail, followed by 30 min of incubation on ice. After centrifugation at 13000 g for 30 min at 4 °C, the supernatant was collected and equally divided into 1.5 mL microcentrifuge tubes. Subsequently, 5 μg of Chk1 antibody (#32531, Abcam) or IgG antibody (#12–370, Sigma-Aldrich) was added to each tube, followed by a 2-h incubation at room temperature. 1:100 of the Dynabeads Protein G (#10004D, Invitrogen) added into each sample, rotated overnight at 4 °C. Separated beads and supernatant with the magnetic separator and washed the beads three times with IP lysis buffer. Resuspended beads with 50 μL IP lysis buffer, incubated at 95 °C for 5 min and proceed to Western blot analysis.

4.18. DNA fiber assay

For DNA fiber assay, approximately 2 × 106 MDA-MB-231 cells were plated in a 6-well plate and cultured overnight, transfected with control-LNA or ACIL-LNA for 48 h. Cells were pulse-labeled with 100 μM IdU for 30 min, washed with PBS, and treated with DMSO or 500 μM HU for 2 h at 37 °C and incubated with 100 μM CldU for 30 min. Then cells were harvested and resuspended in 500 μL of PBS, lysed cells and spread the DNA fibers on glass slides with the spreading buffer (containing 0.5% sodium dodecyl sulfate, 200 mM Tris-HCl pH 7.4, 50 mM EDTA pH 8), followed by 30-min incubattion at room temperature. The fibers were fixed in methanol/acetic acid (3:1, volume: volume) at −20 °C for 15 min. Incubated slides in 70% ethanol at 4 °C for 1 h. Then immersed the slides in 2.5 N HCl for 1 h and washed with PBS. Blocked with 2% BSA in PBS for 30 min at 37 °C. IdU (1:200, #MA5-24879, Invitrogen) and CldU (1:50, # ab6326, Abcam) primary antibodies were incubated at 4 °C overnight. Washed the slides with stringent buffer (prepared by 10 mM Tris-HCl pH 7.4, 400 mM NaCl, 0.2% Tween 20, 0.2% NP-40) 3 times at room temperature. Then slides were incubated with Alexa Fluor 647 goat anti-rat IgG (1:250, # 4418S, CST) and Alexa Fluor 488 goat anti-mouse IgG (1:500, # 4408S, CST) for 1 h in the dark. Mounted with the anti-fade mounting medium and imaged using a confocal laser-scanning microscope (100 × , TCS-SP5, Leica) with a core data acquisition system (LAS AF Lite, Leica). The DNA fiber length was measured by ImageJ software (NCI/NIH), and conversed the fiber length with the equation of 1 μm = 2.59 Kb.

4.19. Immunofluorescence and immunohistochemistry

Briefly, paraffin-embedded slides were deparaffinized with xylene and dehydrated with graded alcohols. Performed antigen retrieval with 0.01 M citrate buffer (pH = 6.0) and eliminated endogenous peroxidase with 3% hydrogen peroxide. The slides were blocked with 1% BSA in PBS for 30 min at 37 °C. Incubated primary antibodies at 4 °C overnight. Primary antibodies anti-RPA2 (1:100, #109084, Abcam), anti-γ-H2AX (Ser139) (1:100, #2577S or 80312, CST), anti-Ki67 (1:100, #16667, Abcam), anti-pATR (S428) (1:100, #ab178407 Abcam), anti-Chk1 (1:100, #32531, Abcam), anti-RAD51 (1:50, #ab133534, Abcam) were used for immunofluorescence (IF). Washed with PBS, the slides were incubated with fluorescent secondary antibodies of the same species for 1 h at room temperature, then counterstained with DAPI (5 μg/mL, #D9542, Sigma). The evaluate the immunostaining positive cells was evaluated at least in 10 random fields under a confocal laser-scanning microscope (63 × , TCS-SP5, Leica) or fluorescence microscope (20 × , Eclipse Ni-E, Nikon). For immunohistochemistry (IHC), anti-pChk1(S345) (1:100, #58567, Abcam), and anti-Ki67 (1:100, #16667, Abcam) were used as primary antibodies. Washed with PBS, the slides were incubated with secondary antibody kit (GK500710, Gene tech) for 1 h at room temperature. Washed the slides three times with PBS then incubated with DAB solution for 10 min (GK500710, Gene tech). Hematoxylin staining solution (#AR1180-1, Boster) was used to counterstain the tissues. The sections were mounted after dehydrated with gradient alcohol and taken pictures under a 20 × objective (Eclipse Ni-E, Nikon). Staining scores were calculated with staining intensity × proportion of positively stained cells (The staining intensity scaled as 0 = no staining, 1 = light brown, 2 = brown, and 3 = dark brown. The proportion of positively stained cells scale was graded as 0, no positive cells; 1, <25%; 2, 25%–50%; 3, 50%–75%; and 4, >75%).

4.20. TUNEL assay

According to the In Situ Cell Death Detection Kit (#11684817910, Roche), the TUNEL assay was performed with the manufacturer's introduction. The paraffin-embedded slides were deparaffinized with xylene and dehydrated with graded alcohols. Incubated the slides with permeabilization solution and trypsin containing 0.01 N HCl. Placed the

slides into 0.1 M citrate buffer (pH = 6.0) and irradiated the slides with 350 W microwave for 5 min. Washed the slides with PBS and incubated with TUNEL reaction mixture for 60 min at 37 °C. Washed the slides with PBS and stained with the DAPI (5 μg/mL, #D9542, Sigma). Then evaluate the positive cells at least in 10 random fields under a fluorescence microscope (100 × , Eclipse Ni-E, Nikon).

4.21. Animal experiment

2×10^6 MDA-MB-231 cells or MCF-7 cells (previously subcutaneously embedded with estrogen tablets) were injected into the fourth mammary fat pads of four-week-old female BALB/C nude mice (Guangdong Gem-Pharmatech), with six mice allocated per group. When the tumor volume reached about 100 mm^3, PBS and ADM (5 mg/kg, once a week) or CDDP (5 mg/kg, twice a week) was injected intravenously through the tail for 4 weeks. All animal studies were under the ethical regulations approved by Institutional Animal Care and Use Committee of Sun Yat-sen University (project number SYSU-IACUC-2021-000945).

4.22. Statistical analysis

All statistical analyses were performed using SPSS 25.0 (IBM) and Prism 9.0 (GraphPad). Results are presented as mean ± SD or SEM of triplicate experiments, with detailed statistical information provided in the figure legends. For continuous variables, two tailed Students' *t*-test was used to analyze the differences between two groups, one-way ANOVA test followed by Dunnett's multiple comparisons test was used to compare differences among multiple groups. For rank variables, Mann-Whitney test or Kruskal-Wallis test was used for two or three groups. The χ2 test was used for comparing the clinical categorical variables. The correlation of ACIL and pChk1 staining score was performed with nonparametric Spearman correlation. For survival analysis, the Kaplan-Meier curves were utilized to illustrate survival times, the Log-rank tests were used to analyze overall survival in breast cancer patients with low and high expression levels of ACIL. In the Kaplan-Meier plotter database, the gene symbol "LRRC75A-AS1" and the "JetSet best probe set" were selected to search ACIL-associated survival times, "Auto select best cutoff" option was used for splitting patients. *P*-value <0.05 was considered statistically significant.

Data availability

Microarray data are deposited in NCBI Gene Expression Omnibus (GEO) dataset under accession code GSE221222 (composed of GSE221060 and GSE221061).

Ethics approval and consent to participate

All animal experiments were approved by the ethical regulations approved by Institutional Animal Care and Use Committee of Sun Yat-sen University (project number SYSU-IACUC-2021-000945). All human specimens in this study were collected with signed informed consent from the patients and approved by Sun Yat-Sen Memorial Hospital's internal review and ethics board (project number SYSEC-KY-KS-2023-171).

CRediT authorship contribution statement

Rong Luo: Writing – original draft, Validation, Investigation. **Jiannan Wu:** Writing – original draft, Investigation, Conceptualization. **Xueman Chen:** Writing – original draft, Validation, Investigation. **Yulan Liu:** Validation, Investigation. **Dequan Liu:** Validation, Resources, Methodology. **Erwei Song:** Supervision, Resources, Project administration, Funding acquisition, Conceptualization. **Man-Li Luo:** Writing – review & editing, Supervision, Project administration, Methodology, Funding acquisition, Conceptualization.

Declaration of competing interest

The authors declare no conflicts of interest.

Acknowledgements

This work was supported by grants from National Key Research and Development Program of China (2021YFA1300602 (M.L.)), the Natural Science Foundation of China (82330056 (E.S.), 92159303 (E.S.), 81930081 (E.S.), 82073048 (M.L.), 82203085 (X.C.)), Guangdong Science and Technology Department (2023B1212060013, 2020B1212030004), Bureau of Science and Technology of Guangzhou (20212200003 (E.S.)), the Program for Guangdong Introducing Innovative and Enterpreneurial Teams (2019BT02Y198 (E.S.)).

Appendix A. Supplementary data

Supplementary data to this article can be found online at https://doi.org/10.1016/j.cellin.2024.100183.

References

Adriaens, C., Standaert, L., Barra, J., Latil, M., Verfaillie, A., Kalev, P., Boeckx, B., Wijnhoven, P. W., Radaelli, E., & Vermi, W. (2016). p53 induces formation of NEAT1 lncRNA-containing paraspeckles that modulate replication stress response and chemosensitivity. *Nature Medicine, 22*, 861–868.

Bartek, J., & Lukas, J. (2003). Chk1 and Chk2 kinases in checkpoint control and cancer. *Cancer Cell, 3*, 421–429.

Bianco, J. N., Bergoglio, V., Lin, Y.-L., Pillaire, M.-J., Schmitz, A.-L., Gilhodes, J., Lusque, A., Mazières, J., Lacroix-Triki, M., & Roumeliotis, T. I. (2019). Overexpression of Claspin and Timeless protects cancer cells from replication stress in a checkpoint-independent manner. *Nature Communications, 10*, 910.

Branzei, D., & Foiani, M. (2010). Maintaining genome stability at the replication fork. *Nature Reviews Molecular Cell Biology, 11*, 208–219.

Bruno, P. M., Liu, Y., Park, G. Y., Murai, J., Koch, C. E., Eisen, T. J., Pritchard, J. R., Pommier, Y., Lippard, S. J., & Hemann, M. T. (2017). A subset of platinum-containing chemotherapeutic agents kills cells by inducing ribosome biogenesis stress. *Nature Medicine, 23*, 461–471.

Canela, A., Maman, Y., Shar-yin, N. H., Wutz, G., Tang, W., Zagnoli-Vieira, G., Callen, E., Wong, N., Day, A., & Peters, J.-M. (2019). Topoisomerase II-induced chromosome breakage and translocation is determined by chromosome architecture and transcriptional activity. *Molecular Cell, 75*, 252–266. e258.

Chen, X., Luo, R., Zhang, Y., Ye, S., Zeng, X., Liu, J., Huang, D., Liu, Y., Liu, Q., & Luo, M.-L. (2022). Long noncoding RNA DIO3OS induces glycolytic-dominant metabolic reprogramming to promote aromatase inhibitor resistance in breast cancer. *Nature Communications, 13*, 7160.

Cimprich, K. A., & Cortez, D. (2008). Atr: An essential regulator of genome integrity. *Nature Reviews Molecular Cell Biology, 9*, 616–627.

Costanzo, V., Shechter, D., Lupardus, P. J., Cimprich, K. A., Gottesman, M., & Gautier, J. (2003). An ATR- and Cdc7-dependent DNA damage checkpoint that inhibits initiation of DNA replication. *Molecular Cell, 11*, 203–213.

Crook, T. R., Souhami, R. L., & Mclean, A. E. (1986). Cytotoxicity, DNA cross-linking, and single strand breaks induced by activated cyclophosphamide and acrolein in human leukemia cells. *Cancer Research, 46*, 5029–5034.

Duijf, P. H., Nanayakkara, D., Nones, K., Srihari, S., Kalimutho, M., & Khanna, K. K. (2019). Mechanisms of genomic instability in breast cancer. *Trends in Molecular Medicine, 25*, 595–611.

Gaillard, H., García-Muse, T., & Aguilera, A. (2015). Replication stress and cancer. *Nature Reviews Cancer, 15*, 276–289.

Ganzinelli, M., Carrassa, L., Crippa, F., Tavecchio, M., Broggini, M., & Damia, G. (2008). Checkpoint kinase 1 down-regulation by an inducible small interfering RNA expression system sensitized in vivo tumors to treatment with 5-fluorouracil. *Clinical Cancer Research: An Official Journal of the American Association for Cancer Research, 14*, 5131–5141.

Gourley, C., Balmaña, J., Ledermann, J. A., Serra, V., Dent, R., Loibl, S., Pujade-Lauraine, E., & Boulton, S. J. (2019). Moving from poly (ADP-ribose) polymerase inhibition to targeting DNA repair and DNA damage response in cancer therapy. *Journal of Clinical Oncology, 37*, 2257–2269.

Gupta, N., Huang, T.-T., Horibata, S., & Lee, J.-M. (2022). Cell cycle checkpoints and beyond: Exploiting the ATR/CHK1/WEE1 pathway for the treatment of PARP inhibitor–resistant cancer. *Pharmacological Research*, Article 106162.

Han, L., Li, Z., Jiang, Y., Jiang, Z., & Tang, L. (2019). SNHG29 regulates miR-223-3p/CTNND1 axis to promote glioblastoma progression via Wnt/β-catenin signaling pathway. *Cancer Cell International, 19*, 345.

Hanahan, D. (2022). Hallmarks of cancer: New dimensions. *Cancer Discovery, 12*, 31–46.

Hsiao, H.-W., Yang, C.-C., & Masai, H. (2021). Roles of Claspin in regulation of DNA replication, replication stress responses and oncogenesis in human cells. *Genome Instability & Disease, 2*, 263–280.

La, T., Chen, S., Zhao, X. H., Zhou, S., Xu, R., Teng, L., Zhang, Y. Y., Ye, K., Xu, L., & Guo, T. (2023). LncRNA LIMp27 regulates the DNA damage response through p27 in p53-defective cancer cells. *Advanced Science, 10*, Article 2204599.
Lee, J., Kumagai, A., & Dunphy, W. G. (2007). The Rad9-Hus1-Rad1 checkpoint clamp regulates interaction of TopBP1 with ATR. *Journal of Biological Chemistry, 282*, 28036–28044.
Lee, Y. C., Zhou, Q., Chen, J., & Yuan, J. (2016). RPA-binding protein ETAA1 is an ATR activator involved in DNA replication stress response. *Current Biology, 26*, 3257–3268.
Li, S., Wu, D., Jia, H., & Zhang, Z. (2020). Long non-coding RNA LRRC75A-AS1 facilitates triple negative breast cancer cell proliferation and invasion via functioning as a ceRNA to modulate BAALC. *Cell Death & Disease, 11*, 643.
Li, J., Zhao, H., McMahon, A., & Yan, S. (2022). APE1 assembles biomolecular condensates to promote the ATR-Chk1 DNA damage response in nucleolus. *Nucleic Acids Research, 50*, 10503–10525.
Lin, Y., Bai, L., Cupello, S., Hossain, M. A., Deem, B., McLeod, M., Raj, J., & Yan, S. (2018). APE2 promotes DNA damage response pathway from a single-strand break. *Nucleic Acids Research, 46*, 2479–2494.
Liu, L., Chen, Y., Huang, Y., Cao, K., Liu, T., Shen, H., Cui, J., Li, B., Cai, J., Gao, F., & Yang, Y. (2021). Long non-coding RNA ANRIL promotes homologous recombination-mediated DNA repair by maintaining ATR protein stability to enhance cancer resistance. *Molecular Cancer, 20*, 94.
Maréchal, A., & Zou, L. (2015). RPA-coated single-stranded DNA as a platform for post-translational modifications in the DNA damage response. *Cell Research, 25*, 9–23.
Mehlich, D., Łomiak, M., Sobiborowicz, A., Mazan, A., Dymerska, D., Szewczyk, Ł. M., Mehlich, A., Borowiec, A., Prełowska, M. K., & Gorczyński, A. (2021). MLK4 regulates DNA damage response and promotes triple-negative breast cancer chemoresistance. *Cell Death & Disease, 12*, 1111.
Mordes, D. A., Glick, G. G., Zhao, R., & Cortez, D. (2008). TopBP1 activates ATR through ATRIP and a PIKK regulatory domain. *Genes & Development, 22*, 1478–1489.
Nguyen, M. N., & Than, V. T. (2024). RNA therapeutics in cancer treatment. *Progress in molecular biology and translational science, 203*, 197–223.
Ni, W., Mo, H., Liu, Y., Xu, Y., Qin, C., Zhou, Y., Li, Y., Li, Y., Zhou, A., Yao, S., et al. (2021). Targeting cholesterol biosynthesis promotes anti-tumor immunity by inhibiting long noncoding RNA SNHG29-mediated YAP activation. *Molecular Therapy: The Journal of the American Society of Gene Therapy, 29*, 2995–3010.
Okamoto, Y., Abe, M., Mu, A., Tempaku, Y., Rogers, C. B., Mochizuki, A. L., Katsuki, Y., Kanemaki, M. T., Takaori-Kondo, A., & Sobeck, A. (2021). SLFN11 promotes stalled fork degradation that underlies the phenotype in Fanconi anemia cells. *Blood, 137*, 336–348.
Olson, E., Nievera, C. J., Klimovich, V., Fanning, E., & Wu, X. (2006). RPA2 is a direct downstream target for ATR to regulate the S-phase checkpoint. *Journal of Biological Chemistry, 281*, 39517–39533.
Petermann, E., Orta, M. L., Issaeva, N., Schultz, N., & Helleday, T. (2010). Hydroxyurea-stalled replication forks become progressively inactivated and require two different RAD51-mediated pathways for restart and repair. *Molecular Cell, 37*, 492–502.
Pilié, P. G., Tang, C., Mills, G. B., & Yap, T. A. (2019). State-of-the-art strategies for targeting the DNA damage response in cancer. *Nature Reviews Clinical Oncology, 16*, 81–104.
Rao, Q., Liu, M., Tian, Y., Wu, Z., Hao, Y., Song, L., Qin, Z., Ding, C., Wang, H.-W., & Wang, J. (2018). Cryo-EM structure of human ATR-ATRIP complex. *Cell Research, 28*, 143–156.
Saldivar, J. C., Cortez, D., & Cimprich, K. A. (2017). The essential kinase ATR: Ensuring faithful duplication of a challenging genome. *Nature Reviews Molecular Cell Biology, 18*, 622–636.
Sartori, A. A., Lukas, C., Coates, J., Mistrik, M., Fu, S., Bartek, J., Baer, R., Lukas, J., & Jackson, S. P. (2007). Human CtIP promotes DNA end resection. *Nature, 450*, 509–514.
Shiotani, B., & Zou, L. (2009). Single-stranded DNA orchestrates an ATM-to-ATR switch at DNA breaks. *Molecular Cell, 33*, 547–558.
Simoneau, A., & Zou, L. (2021). An extending ATR–CHK1 circuitry: The replication stress response and beyond. *Current Opinion in Genetics & Development, 71*, 92–98.
Sirbu, B. M., Couch, F. B., Feigerle, J. T., Bhaskara, S., Hiebert, S. W., & Cortez, D. (2011). Analysis of protein dynamics at active, stalled, and collapsed replication forks. *Genes & Development, 25*, 1320–1327.
Smits, V. A., Cabrera, E., Freire, R., & Gillespie, D. A. (2019). Claspin–checkpoint adaptor and DNA replication factor. *FEBS Journal, 286*, 441–455.
Toledo, L. I., Altmeyer, M., Rask, M.-B., Lukas, C., Larsen, D. H., Povlsen, L. K., Bekker-Jensen, S., Mailand, N., Bartek, J., & Lukas, J. (2013). ATR prohibits replication catastrophe by preventing global exhaustion of RPA. *Cell, 155*, 1088–1103.
Van Nostrand, E. L., Pratt, G. A., Shishkin, A. A., Gelboin-Burkhart, C., Fang, M. Y., Sundararaman, B., Blue, S. M., Nguyen, T. B., Surka, C., & Elkins, K. (2016). Robust transcriptome-wide discovery of RNA-binding protein binding sites with enhanced CLIP (eCLIP). *Nature Methods, 13*, 508–514.
Vassin, V. M., Anantha, R. W., Sokolova, E., Kanner, S., & Borowiec, J. A. (2009). Human RPA phosphorylation by ATR stimulates DNA synthesis and prevents ssDNA accumulation during DNA-replication stress. *Journal of Cell Science, 122*, 4070–4080.
Wang, L., Li, J., Zhou, H., Zhang, W., Gao, J., & Zheng, P. (2021). A novel lncRNA Discn fine-tunes replication protein A (RPA) availability to promote genomic stability. *Nature Communications, 12*, 5572.
Wheeler, D. L., Church, D. M., Federhen, S., Lash, A. E., Madden, T. L., Pontius, J. U., Schuler, G. D., Schriml, L. M., Sequeira, E., Tatusova, T. A., & Wagner, L. (2003). Database resources of the national center for Biotechnology. *Nucleic Acids Research, 31*, 28–33.
Winkle, M., El-Daly, S. M., Fabbri, M., & Calin, G. A. (2021). Noncoding RNA therapeutics - challenges and potential solutions. *Nature Reviews Drug Discovery, 20*, 629–651.
Wu, X., Xu, S., Wang, P., Wang, Z. Q., Chen, H., Xu, X., & Peng, B. (2022). ASPM promotes ATR-CHK1 activation and stabilizes stalled replication forks in response to replication stress. *Proceedings of the National Academy of Sciences of the U S A, 119*, Article e2203783119.
Yang, C.-C., Suzuki, M., Yamakawa, S., Uno, S., Ishii, A., Yamazaki, S., Fukatsu, R., Fujisawa, R., Sakimura, K., & Tsurimoto, T. (2016). Claspin recruits Cdc7 kinase for initiation of DNA replication in human cells. *Nature Communications, 7*, Article 12135.
Yazinski, S. A., & Zou, L. (2016). Functions, regulation, and therapeutic implications of the ATR checkpoint pathway. *Annual Review of Genetics, 50*.
Zeman, M. K., & Cimprich, K. A. (2014). Causes and consequences of replication stress. *Nature Cell Biology, 16*, 2–9.
Zhang, Y., He, Q., Hu, Z., Feng, Y., Fan, L., Tang, Z., Yuan, J., Shan, W., Li, C., & Hu, X. (2016). Long noncoding RNA LINP1 regulates repair of DNA double-strand breaks in triple-negative breast cancer. *Nature Structural & Molecular Biology, 23*, 522–530.
Zhang, Y., & Hunter, T. (2014). Roles of Chk1 in cell biology and cancer therapy. *International Journal of Cancer, 134*, 1013–1023.
Zhao, W., Wiese, C., Kwon, Y., Hromas, R., & Sung, P. (2019). The BRCA tumor suppressor network in chromosome damage repair by homologous recombination. *Annual Review of Biochemistry, 88*, 221.
Zhou, B.-B. S., & Bartek, J. (2004). Targeting the checkpoint kinases: Chemosensitization versus chemoprotection. *Nature Reviews Cancer, 4*, 216–225.
Zou, L., & Elledge, S. J. (2003). Sensing DNA damage through ATRIP recognition of RPA-ssDNA complexes. *Science, 300*, 1542–1548.